

Harnessing Non-Boltzmann Steady States in Lanthanide Nanocrystals for Mid-Infrared Optoelectronics

Xinyang Yu^{1,2}, Yin Huang¹, Karin Yamamura^{1,2}, Chenyi Wang³, Lei Ding⁴, Mehran Kianinia^{1,2}, Yang Yu⁵, Jiyun Kim^{1,2}, Baolei Liu⁶, Xiaoxue Xu⁷, Otto Cranwell Schaeper^{1,2}, Yue Bian⁵, Lan Fu⁵, Guochen Bao¹, Qian Peter Su⁷, Fan Wang³, Igor Aharonovich^{1,2*}, Chaohao Chen^{1,2,7*}

¹ School of Mathematical and Physical Sciences, Faculty of Science, The University of Technology Sydney, Ultimo, NSW 2007, Australia

² Australian Research Council Centre of Excellence for Transformative Meta-Optical Systems, The University of Technology Sydney, Ultimo, NSW 2007, Australia

³ Science and Technology Center for Quantum Biology, National Institute of Extremely-Weak Magnetic Field Infrastructure, Hangzhou, China

⁴ Centre for Atomaterials and Nanomanufacturing, School of Science, RMIT University, Melbourne, Victoria, Australia

⁵ Australian Research Council Centre of Excellence for Transformative Meta-Optical Systems, Department of Electronic Materials Engineering, Research School of Physics, The Australian National University, Canberra ACT 2600, Australia

⁶ School of Electrical and Data Engineering, Faculty of Engineering and Information Technology, The University of Technology Sydney, Sydney, NSW 2007, Australia

⁷ School of Biomedical Engineering, Faculty of Engineering and Information Technology, The University of Technology Sydney, Sydney, NSW 2007, Australia

* Correspondence to: Igor.Aharonovich@uts.edu.au; Chaohao.Chen@uts.edu.au

Abstract

Converting mid-infrared (MIR) radiation to visible or near-infrared wavelengths is essential for imaging and sensing, yet achieving sensitive, low-power, and scalable detection remains challenging. Lanthanide nanocrystals provide an alternative through ratiometric luminescence but are typically constrained by Boltzmann statistics, which tie population distributions to lattice temperature and limit signal contrast. Here we show that MIR irradiation rebalances dissipative relaxation pathways, driving lanthanide emitters into a non-Boltzmann steady state that enables non-thermal control of population distributions. This allows emission behaviours inaccessible under thermal equilibrium. We exploit this regime to achieve linear MIR detection with respect to MIR power across 6.8–8.6 μm . The ratiometric response is intrinsically independent of the pump power, enabling operation at an ultralow excitation power of 10 μW , several orders of magnitude lower than conventional approaches. Using standard silicon photodetectors, we then demonstrate room-temperature MIR imaging with detection limits approaching 4 nW μm^{-2} . Our results establish lanthanide nanoparticles as an efficient platform for MIR conversion and sensing in nanophotonic systems.

Introduction

Mid-infrared (MIR) detection is essential for many practical technologies because MIR photons encode rich molecular vibrational and thermal information.^{1,2} Applications including chemical sensing³ and environmental monitoring⁴ and biomedical diagnostics⁵ rely on sensitive detection of MIR radiation. However, the development of MIR detectors has lagged behind their visible and near-infrared counterparts because MIR photons carry low energies that are poorly matched to conventional semiconductor bandgaps.^{6,7} Further, MIR detectors are costly, bulky and inefficient. As a result, high-performance MIR photodetectors often require cryogenic cooling or complex device architectures involving sophisticated nanofabrication.

Spectral conversion, therefore, offers an attractive alternative by upconverting MIR signals into visible or near-infrared photons that can be efficiently detected using commercially available silicon photodetectors.^{8,9,10,11} Most MIR-to-visible conversion approaches rely on nonlinear optical processes requiring phase matching in bulky crystals or strong field confinement in resonant nanocavities,^{12,13,14} which limits scalability and practical applications.

Luminescent nanotransducers based on lanthanide nanocrystals provide a promising route for MIR spectral conversion at room temperature because their shielded 4f electronic manifolds support spectrally stable and narrowband emissions.^{15,16,17,18,19} Stark splitting further creates closely spaced sublevels with energy separations in the MIR range.^{20,21} Steady-state emission in thermally coupled lanthanide manifolds follows Boltzmann statistics, which fixes the population distribution between closely spaced excited states through thermal equilibrium.^{22,23,24,25,26} Consequently, emission ratios are intrinsically linked to lattice temperature and cannot be tuned independently of thermal conditions, imposing a fundamental constraint on dynamic control and signal contrast. Previous strategies have attempted to modify emission ratios through excitation pathways²⁷, pump-power modulation²⁸ or thermal perturbations.²⁹ However, these approaches preserve Boltzmann-governed steady states because phonon-mediated relaxation continuously restores thermal equilibrium between thermally coupled manifolds.

Here we show that MIR irradiation rebalances dissipative relaxation pathways, driving lanthanide emitters into a non-Boltzmann steady state in which population distributions are no longer governed by lattice temperature. This enables non-thermal control of steady-state populations and gives rise to emission behaviours inaccessible under thermal equilibrium. As a result, the thermally coupled green emission bands exhibit opposite intensity modulation together with strongly state-selective lifetime renormalization inconsistent with uniform heating. Exploiting this non-Boltzmann steady state, we demonstrate linear response to MIR intensity with pump-power-independent ratiometric detection across 6.8–8.6 μm . A detection limit of 4 nW μm^{-2} is achieved. Notably, the sensing mechanism operates under less than 10 μW near-infrared excitation several orders of magnitude lower than conventional approaches. We also utilise this effect to realise room-temperature MIR imaging using standard silicon photodetectors. These results establish MIR photon-driven kinetic rebalancing as a route for controlling steady-state populations beyond Boltzmann constraints in lanthanide photonics.

Results

Breaking Boltzmann steady-state balance in thermally coupled manifolds

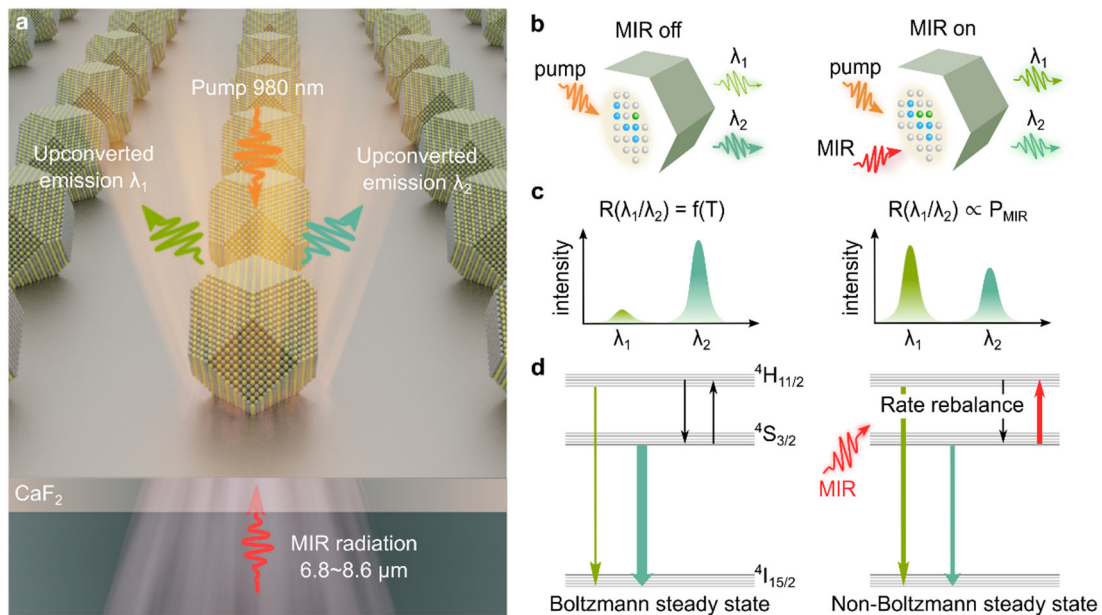


Figure 1 | Non-Boltzmann steady-state reconfiguration in thermally coupled manifolds. *a*, Conceptual illustration of MIR-driven upconversion. A near-infrared pump excites lanthanide-doped nanoparticles on a CaF₂ substrate, producing two spectrally resolved visible emission channels (λ_1 and λ_2). Continuous-wave mid-infrared (MIR) radiation (6.8–8.6 μm) is simultaneously applied, interacting with the phonon-mediated relaxation processes in the host lattice. **b**, Steady-state emission under MIR off (left) and MIR on (right) conditions. In the absence of MIR irradiation, population redistribution within thermally coupled manifolds follows thermodynamic equilibrium. Under MIR illumination, the relative populations of the two emitting states are modified, leading to opposite intensity changes. **c**, Functional dependence of the emission ratio $R = I_{\lambda_1}/I_{\lambda_2}$ is governed by temperature, consistent with Boltzmann statistics $\ln(R) \propto -\Delta E/kT$. Under MIR irradiation, the ratio becomes dependent on MIR power intensity $R \propto P_{\text{MIR}}$, indicating departure from purely thermal control. **d**, Mechanism of steady-state reconfiguration in Er³⁺ ions. In the Boltzmann steady state, forward and backward nonradiative transitions between thermally coupled levels establish a temperature-defined population ratio. MIR irradiation modifies phonon-assisted relaxation rates between these levels, likely through coupling to vibrational modes in the host lattice, thereby rebalancing the transition rates and driving the system into a non-Boltzmann steady state without altering the electronic level structure.

In thermally coupled lanthanide manifolds, phonon-assisted relaxation establishes a steady-state population balance between closely spaced excited levels. Under thermal equilibrium, the population ratio follows the Boltzmann dynamics, so that the corresponding emission ratio is determined by temperature. The MIR sensing concept explored in this work is illustrated in **Fig. 1a**. The lanthanide-doped nanocrystals are deposited on a CaF₂ substrate and excited by a

near-infrared pump to generate two spectrally separated upconversion emission channels. Continuous-wave MIR radiation is simultaneously applied, introducing an additional perturbation that interacts with the phonon-mediated relaxation processes of the excited states.

The steady-state emission behaviour in Erbium ions (Er^{3+}) is compared in **Fig. 1b**.³⁰ Without MIR irradiation, population exchange within the thermally coupled manifold follows thermodynamic equilibrium, $I_{\lambda_1}/I_{\lambda_2} \propto \exp(-\Delta E/kT)$, which results in a fixed emission ratio between the two bands determined by temperature. Under MIR illumination, the relaxation dynamics are modified and the two emission intensities evolve in opposite directions. Consequently, the emission ratio transitions from a temperature-governed dependence consistent with Boltzmann statistics (**Fig. 1c**) to a regime that depends on MIR intensity. This behaviour originates from MIR-induced perturbation of the relaxation pathways between the excited states. As illustrated schematically in **Fig. 1d**, MIR irradiation selectively rebalances phonon-assisted transitions within the manifold, disrupting the detailed balance that normally maintains thermal equilibrium and driving the system into a non-Boltzmann steady state.

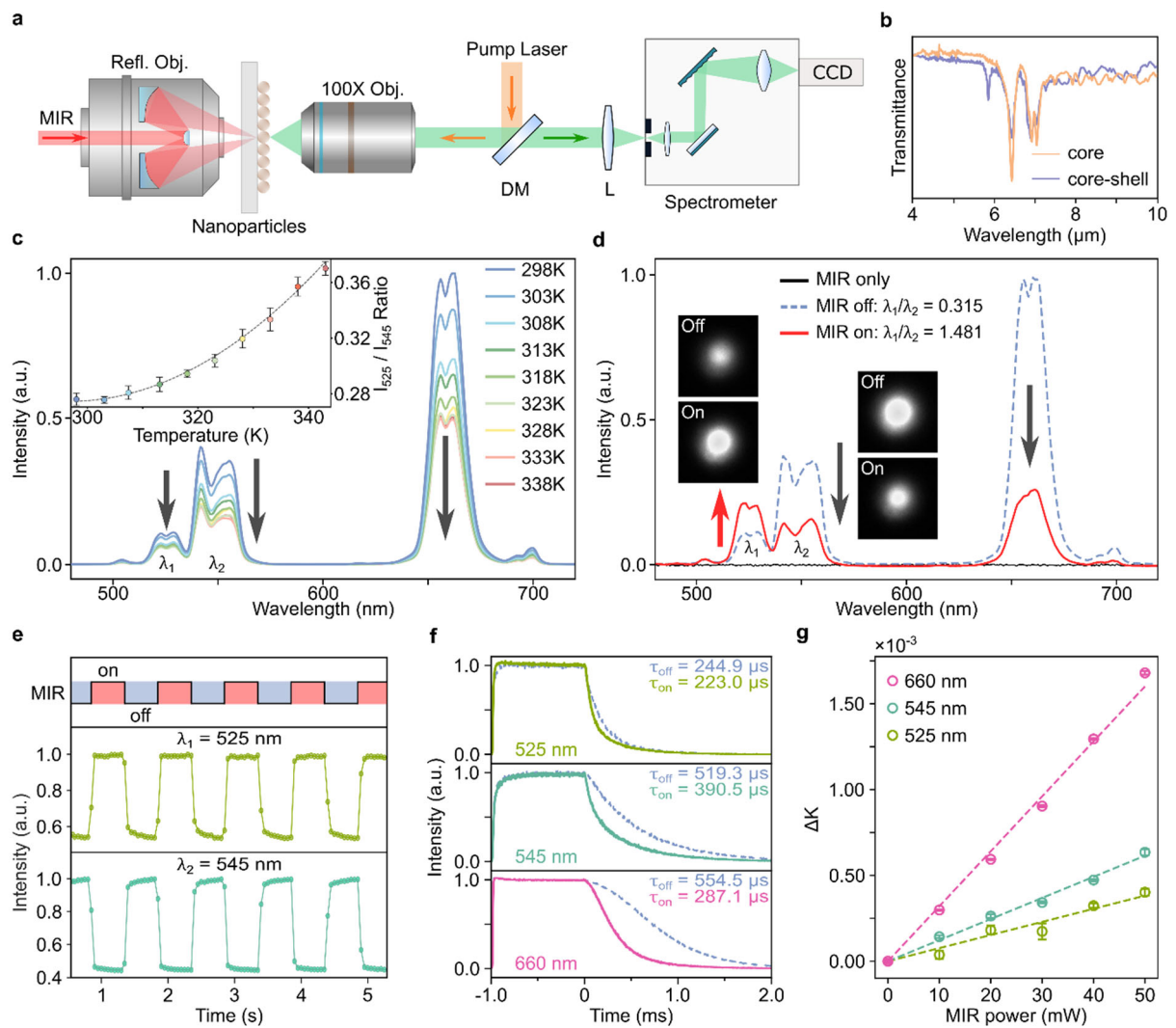


Figure 2 | *Experimental validation of MIR-driven non-Boltzmann steady-state redistribution.* **a**, Schematic for MIR-modulated upconversion measurements. A tunable MIR

quantum cascade laser illuminates the nanocrystal ensemble while a 980 nm pump drives $\text{Yb}^{3+}/\text{Er}^{3+}$ upconversion. The converted visible emission is collected and analysed by the spectrometer. **b**, FTIR absorption spectrum of the nanocrystals. **c**, Thermal baseline measurement. Increasing temperature from 298 K to 338 K produces synchronous decrease of the 525 nm and 545 nm emission bands, while the intensity ratio changes only from 0.28 to 0.38, consistent with Boltzmann-governed population redistribution. **d**, MIR-induced modulation under identical pumping conditions. MIR illumination enhances the 525 nm emission while suppressing the 545 nm band, producing a pronounced ratiometric contrast I_{525}/I_{545} : 0.32 \rightarrow 1.48. Insets show corresponding upconversion images highlighting the MIR-induced ratiometric change. **e**, Time-domain modulation of the 525 and 545 nm intensities under periodic MIR on/off illuminations. **f**, Time-resolved photoluminescence under 7.4 μm MIR irradiation at 50 mW. The ${}^4\text{H}_{11/2}$ (525 nm) lifetime changes marginally ($\sim 8.9\%$), whereas the ${}^4\text{S}_{3/2}$ (545 nm) and $4\text{F}_{9/2}$ (660 nm) lifetimes shorten by $\sim 24\%$ and $\sim 48.2\%$, respectively. **g**, MIR-power-dependent lifetime renormalization. The change in inverse lifetime ($\Delta K = 1/\tau - 1/\tau_0$) scales linearly with MIR power, consistent with an additional relaxation channel whose rate increases proportionally with MIR intensity.

To experimentally verify the MIR-induced deviation from Boltzmann-governed steady-state populations, we build a dual-wavelength excitation platform, as illustrated in **Supplementary Note 1** and **Fig. S1**. Under 980 nm excitation, **Supplementary Fig. S2** demonstrates Yb^{3+} sensitizers absorb pump photons and transfer energy to Er^{3+} ions, populating excited states within the Er^{3+} manifold that generate the characteristic green and red upconversion emission bands. A $\text{NaYF}_4: 20\%\text{Yb}^{3+}/2\%\text{Er}^{3+}$ nanocrystal film (see synthesis detail in **Supplementary Note 2**) was simultaneously illuminated by a 980 nm pump laser and a tunable MIR quantum cascade laser as shown in **Fig. 2a**. The two beams were incident from opposite directions and spatially overlapped within the nanoparticle film, enabling controlled perturbation of the excited-state relaxation dynamics while maintaining constant optical excitation. Transmission electron microscopy confirms monodisperse nanocrystals with an average diameter of ~ 34 nm (**Supplementary Fig. S3**), suitable for ensemble characterization. Fourier-transform infrared spectroscopy further reveals broadband MIR absorption spanning 4.6-10.5 μm (**Fig. 2b**). The spectral profile closely matches the experimentally extracted MIR sensitivity derived from ratiometric modulation measurements, indicating that the observed response originates from intrinsic photon absorption within the nanoparticle system rather than extrinsic heating.

To distinguish non-thermal effects from conventional heating, we first established a temperature-dependent baseline. As shown in **Fig. 2c**, increasing the sample temperature from 298 K to 338 K leads to a simultaneous decrease of emission intensities across all bands (525 nm, 545 nm and 660 nm), due to the enhanced nonradiative relaxation. The intensity ratio between the two green emissions (I_{525}/I_{545}) increased only slightly from 0.28 to 0.38 (**Fig. 2c** inset). This behaviour originates from thermally activated population redistribution within the thermally coupled ${}^4\text{S}_{3/2}$ and ${}^4\text{H}_{11/2}$ manifolds, where phonon-assisted transitions enable upward population transfer to the higher-energy state. As a result, the population ratio follows a Boltzmann distribution, establishing the thermodynamic limit of emission modulation under equilibrium conditions. In contrast, MIR illumination drives the two thermally coupled

emissions in opposite directions. As illustrated in **Figure 2d**, the 525 nm emission increases while the 545 nm emission decreases, producing a ratio change from 0.32 to 1.48 that far exceeds the thermally accessible range. Infrared thermal imaging under identical MIR power shows a maximum temperature rise to ~ 335 K (**Supplementary Fig. S4 and S5**), confirming that the observed modulation cannot be attributed to heating.

Further insight is obtained from dynamic measurements. Under periodic MIR on/off excitation, the two green bands respond reversibly with opposite phases, as shown in **Fig. 2e**, demonstrating direct modulation of excited-state populations rather than thermally driven redistribution. **Fig. 2f** indicates that the time-resolved photoluminescence measurements reveal strongly state-selective lifetime renormalization. The lifetime of the $^4\text{H}_{11/2}$ level (525 nm) changes only marginally ($\sim 8.9\%$), whereas the $^4\text{S}_{3/2}$ lifetime (545 nm) decreases by $\sim 24\%$. An even stronger reduction ($\sim 48.2\%$) is observed for the lower $^4\text{F}_{9/2}$ level (~ 660 nm), which is populated through different relaxation pathways. Such a pronounced hierarchy of lifetime modification is inconsistent with uniform heating, which would affect all manifolds similarly. Instead, it indicates selective modification of nonradiative relaxation pathways within the excited-states.

The MIR-induced change in inverse lifetime, $\Delta K = \frac{1}{\tau(P) - 1/\tau_0}$, where $\tau(P)$ and τ_0 denote the lifetimes measured with and without MIR irradiation, respectively, exhibits a linear dependence on MIR power P_{MIR} (**Fig. 2g** and **Supplementary Fig. S6**). Here $K = 1/\tau$ represents the total decay rate. This behaviour is consistent with an additional photon-driven relaxation channel, such that:

$$\frac{1}{\tau(P)} = \frac{1}{\tau_0} + \alpha P_{\text{MIR}}$$

where α describes the MIR-induced rate coefficient associated with photon-assisted relaxation processes.

Within a rate-equation framework in **Supplementary Note 3**, these observations can be reproduced by introducing a state-dependent MIR-driven relaxation term that selectively enhances depopulation of the $^4\text{S}_{3/2}$ and $^4\text{F}_{9/2}$ levels while minimally perturbing the $^4\text{H}_{11/2}$ state. Such non-uniform rate modification disrupts the detailed balance that normally governs thermal exchange within the thermally coupled manifold. Consequently, the steady-state population distribution becomes externally controllable through photon-driven rate rebalancing rather than being uniquely determined by temperature ($\sim \Delta E/kT$). Numerical simulations based on this model reproduce both the opposite-sign intensity modulation and the observed lifetime hierarchy (**Supplementary Fig. S7**), supporting the emergence of a non-Boltzmann steady state.

Pump power independent sensing enabled by non-Boltzmann steady states

To further examine how MIR irradiation modifies the excited-state dynamics, we investigated the pump-power dependence of the two green emission bands. In the absence of MIR

illumination, both the 525 nm ($^4H_{11/2}$) and 545 nm ($^4S_{3/2}$) emissions increase nonlinearly with pump power, while still remaining strongly correlated. As illustrated in **Fig. 3a**, this behaviour reflects conventional upconversion dynamics, where excitation density governs the population flow through intermediate states. In contrast, under MIR irradiation the two thermally coupled bands exhibit opposite responses. The 525 nm emission increases whereas the 545 nm emission decreases with increasing pump power. Consequently, the emission ratio deviates strongly from the equilibrium behaviour. As shown in **Figure 3b and Supplementary Fig. S8&S9**, the ratiometric signal shifts to a higher plateau under MIR irradiation and remains nearly constant across the entire excitation range from 10 μ W to 500 mW.

Importantly, the overall pump dependence of the individual emission intensities is otherwise preserved, indicating that MIR irradiation primarily perturbs the relaxation pathways rather than the excitation processes. As a result, the ratiometric signal becomes largely independent of excitation density over three orders of magnitude of pump power (10-1000 μ W), as shown in **Fig. 3c**. This excitation-independent behaviour directly reflects the emergence of a non-Boltzmann steady state in which the population distribution is governed by photon-driven rate rebalance rather than by excitation-controlled kinetics.

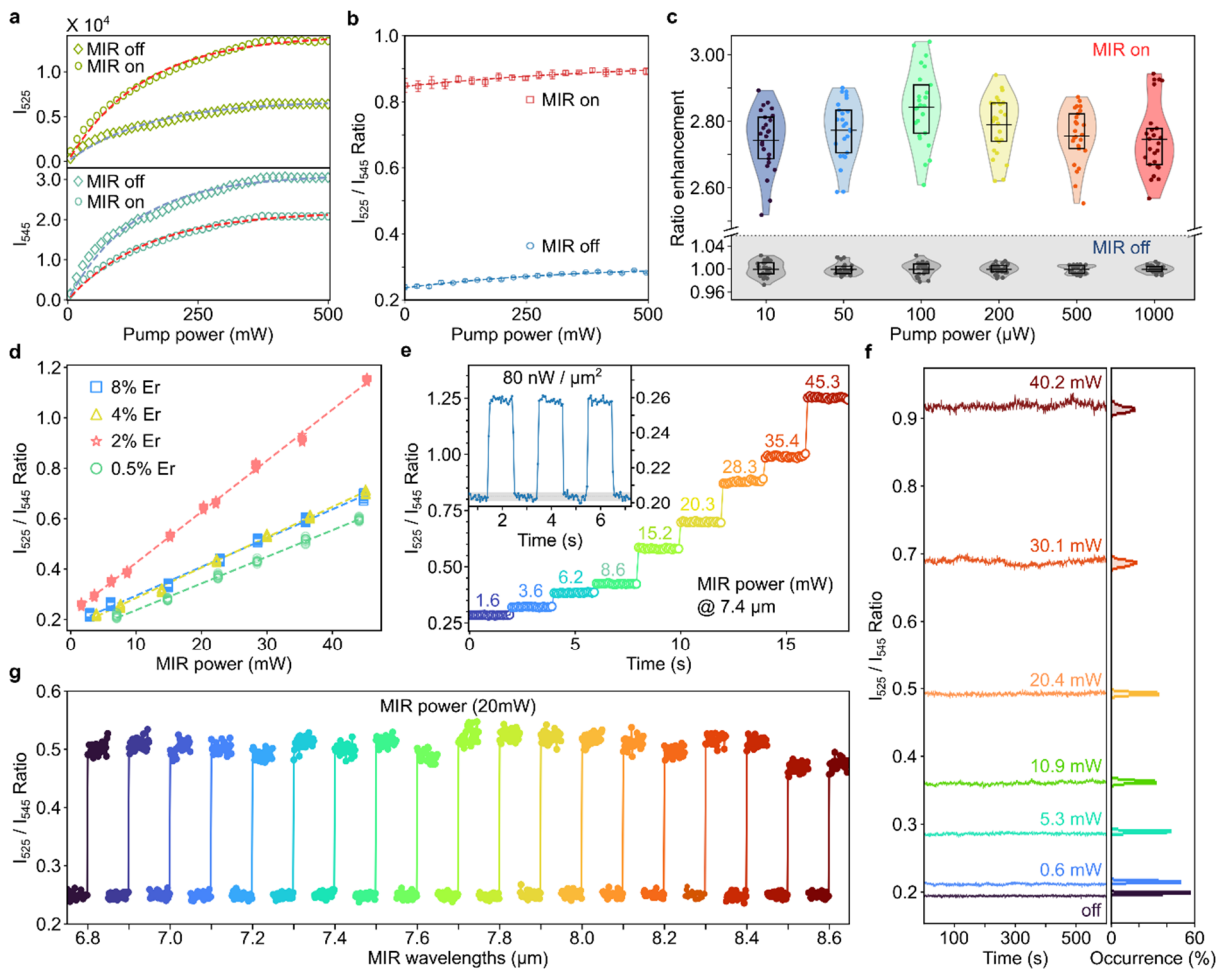


Figure 3 | Excitation-decoupled response of the MIR-driven non-Boltzmann steady state. a, Pump-power dependence of the 525 nm and 545 nm emission bands with and without MIR irradiation. MIR illumination induces opposite intensity changes in the two thermally coupled

bands across the entire excitation range. **b**, Emission ratio as a function of 980 nm pump power under MIR on and off conditions. **c**, Statistical distribution of the ratiometric enhancement across pump powers spanning the weak-excitation regime (10–1000 μW). **d**, MIR-induced ratiometric response for nanocrystals with varying Er^{3+} concentrations (0.5–8%). **e**, Linear dependence of the emission ratio on MIR power under constant excitation, with representative temporal modulation (inset). The detection limit is estimated to be 4 $\text{nW } \mu\text{m}^{-2}$ at 7.4 μm , defined by a signal-to-noise ratio of 1 (see Supplementary Note 4). **f**, Distribution of the ratiometric signal under different MIR power densities, illustrating the progressive increase of I_{525}/I_{545} with increasing MIR intensity. **g**, Broadband ratio response as a function of MIR wavelength (6.8–8.6 μm).

The robustness of this regime was further examined across different Er^{3+} concentrations ranging from 0.5% to 8%, as shown in **Fig. 3d**. Although the absolute emission ratios vary due to concentration-dependent energy-transfer dynamics, the MIR-induced modulation remains linear in all samples, confirming that the mechanism is not restricted to a specific doping condition. Comparison between bare-core and core–shell nanocrystals (**Supplementary Fig. S10**) shows that both structures retain a linear response to MIR power, while the core–shell samples exhibit a reduced modulation amplitude. This suggests that the shell modifies the local vibrational environment and reduces the coupling between MIR-driven perturbations and the excited-state relaxation network. At fixed 980 nm excitation, **Fig. 3e** illustrates the emission ratio increases linearly with MIR power, with rapid and reversible switching under periodic MIR modulation. This linear dependence is consistent with an additional MIR-introduced relaxation rate proportional to MIR intensity, as expected for a first-order perturbation to the steady-state population balance. The inset shows the reliably detected MIR power densities below 80 $\text{nW } \mu\text{m}^{-2}$ with a detection limit of $\sim 4 \text{ nW } \mu\text{m}^{-2}$, defined by a signal-to-noise ratio of 1 from the linear calibration of the MIR response (see **Supplementary Note 4**). This performance is consistent with the enhanced sensitivity enabled by the non-Boltzmann steady state. The statistical robustness of the ratiometric signal is further illustrated in **Fig. 3f**. As the MIR intensity increases, the emission ratio shifts to higher values while maintaining narrow distributions, enabling reliable discrimination between different MIR power levels.

To further examine the spectral characteristics of this mechanism, we measured the MIR response across different wavelengths. As shown in **Fig. 3g**, the ratiometric signal persists across the 6.8–8.6 μm range, demonstrating broadband sensitivity within the accessible spectral window. At each wavelength, the emission ratio increases linearly with MIR power (**Supplementary Fig. S11**), indicating that the MIR-induced relaxation perturbation remains proportional to the incident MIR intensity. The smooth spectral dependence is consistent with the intrinsic mid-infrared absorption of the nanocrystal system revealed by FTIR measurements, supporting a direct coupling between MIR excitation and excited-state relaxation dynamics rather than indirect thermal effects. The accessible spectral range explored here is limited by the tuning range of the QCL source, while the broadband absorption of the nanocrystals suggests the possibility of extending the operational bandwidth over a much wider MIR region. The nanoparticles also exhibit excellent photostability. Under continuous 980 nm excitation with MIR co-irradiation, the emission ratio from a fixed spot remains stable for over 5 hours

with a standard deviation of 3.74%, comparable to the <3% power fluctuation of the QCL source (**Supplementary Fig. S12**).

To demonstrate the practical utility of the non-Boltzmann steady state, we integrated the lanthanide nanocrystal film with a silicon photodetector for MIR imaging. MIR irradiation modulates the upconversion emission, which was spectrally filtered using a 660 nm band-pass filter corresponding to the strongest emission band and detected as a voltage change ΔV . For these measurements, the MIR beam was mechanically chopped at 100 Hz and the signal was extracted using lock-in detection to improve the signal-to-noise ratio, as shown in **Supplementary Fig. S1**. **Figure 4a** shows a two-dimensional map of ΔV as a function of MIR and pump power, revealing a clear electrical response of the nanocrystal film.

The electrical signal increases linearly with MIR power across different pump powers, as illustrated in **Fig. 4b** and **Supplementary Fig. S13**. The time-resolved traces in **Fig. 4c** shows stable and reproducible modulation under stepwise MIR excitation, demonstrating reliable MIR detection under dynamic illumination. Because the MIR beam is mechanically modulated at 100 Hz while the 980 nm excitation remains continuous, the observed modulation frequency is determined by the measurement scheme rather than by the intrinsic response of the nanocrystal system. The underlying excited-state dynamics occur on microsecond timescales as shown in **Fig. 2f**, indicating that substantially faster detection bandwidths could be supported.

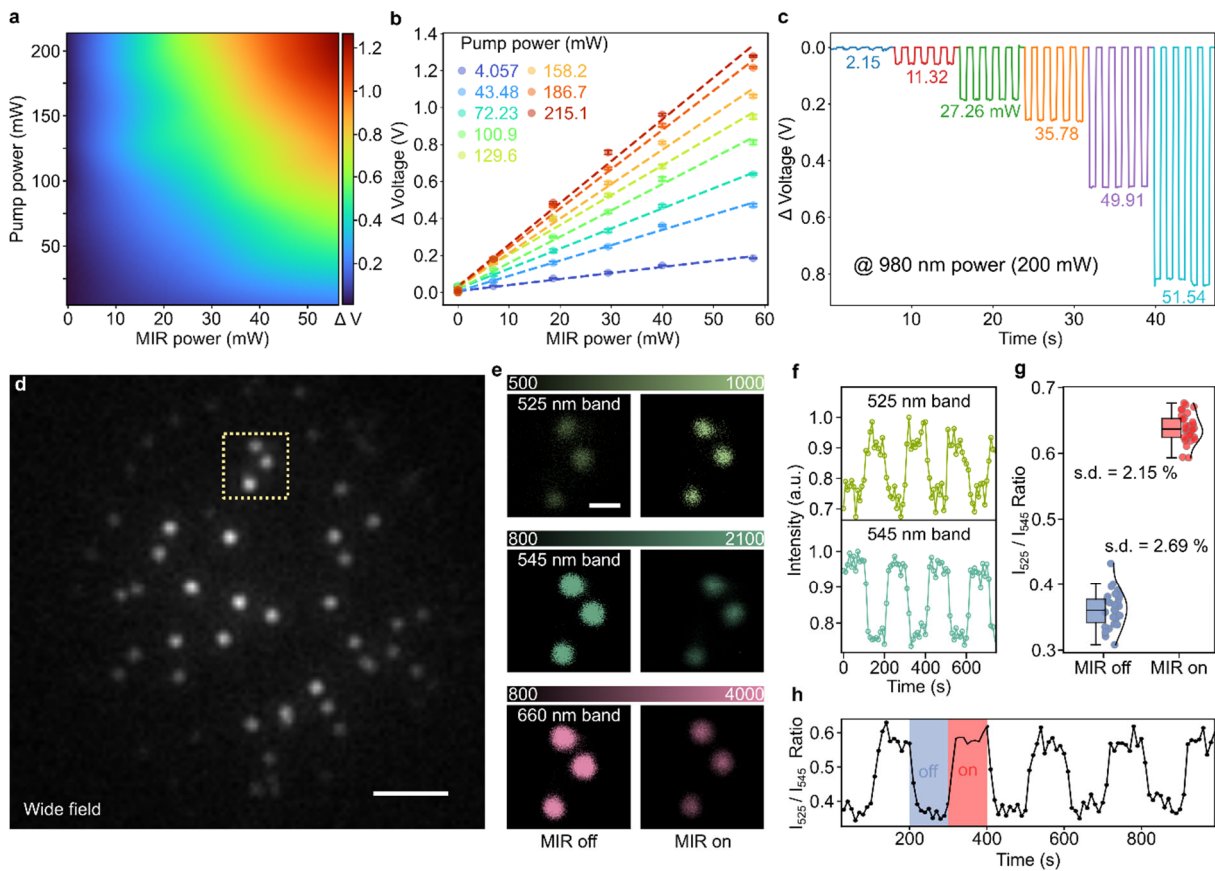


Figure 4 | MIR detection and single-particle imaging enabled by non-Boltzmann upconversion dynamics. a, Electrical response of the lanthanide nanocrystal film integrated

with a silicon photodetector. The colour map shows the measured voltage change ΔV as a function of MIR power and pump power under 650 nm emission detection, demonstrating electrical readout of MIR-induced modulation. **b**, Linear dependence of the electrical response ΔV on MIR power measured at different pump powers, demonstrating tunable MIR sensitivity. **c**, Time-resolved electrical signal under stepwise MIR excitation, showing stable and reproducible modulation during repeated MIR on–off cycles. **d**, Wide-field fluorescence image of sparsely dispersed nanocrystals used for single-particle measurements. The dashed region highlights representative emitters. Scale bars, 5 μm . **e**, The representative single-particle emission images in different spectral channels (525 nm, 545 nm and 660 nm) with MIR off and on. The thermally coupled green bands exhibit opposite intensity changes under MIR illumination. Scale bars, 1 μm . **f**, Time-resolved emission intensity from a representative single nanocrystal measured in the 525 nm and 545 nm spectral bands under periodic MIR excitation. **g**, Statistical distribution of the single-particle ratiometric response (I_{525}/I_{545}) with and without MIR illumination, demonstrating consistent ratiometric contrast across individual emitters. **h**, Time-resolved ratiometric signal from an individual nanocrystal showing reversible modulation under periodic MIR excitation.

A comparison with representative MIR upconversion platforms reported in the literature further highlights the advantages of the present system. In contrast to previously reported approaches that typically require milliwatt-level optical excitation or cryogenic operation, the lanthanide nanocrystal platform demonstrated here operates under microwatt-level near-infrared excitation while maintaining room-temperature detection and compatibility with optical imaging architectures. The visible upconversion readout also enables straightforward integration with silicon photodetectors and conventional optical instrumentation. A broader comparison of material systems, working wavelengths, excitation conditions, and imaging capabilities is summarized in **Supplementary Table S1 and Fig. S14**.

The developed MIR co-irradiation scheme can also be extended to single-particle imaging. To this extent, we performed wide-field fluorescence imaging of sparsely dispersed single nanoparticles as illustrated in **Fig. 4d** and **Supplementary Fig. S15**. Under MIR illumination, the thermally coupled green emission bands exhibit opposite responses, with the 525 nm emission increasing while the 545 nm emission decreases, consistent with the ensemble measurements. The red emission band at 660 nm is simultaneously modulated, providing an additional strong intensity channel for electrical readout. **Fig. 4e** shows representative single-particle emission images in the different spectral channels.

Time-resolved traces from individual emitters further reveal reversible modulation of the emission intensities in the 525 nm and 545 nm channels under periodic MIR excitation. **Fig. 4f** demonstrates the corresponding time traces, exhibiting anti-correlated modulation consistent with the non-Boltzmann population redistribution. **Fig. 4g** presents the statistical distribution of the ratiometric response, where the emission ratio I_{525}/I_{545} systematically increases under MIR illumination. Finally, **Fig. 4h** shows that the ratiometric signal from individual nanocrystals can be repeatedly modulated under periodic MIR excitation, indicating that the

non-Boltzmann steady state can be reversibly established without observable degradation over measurement duration.

The results presented here reveal a distinct regime of light-matter interaction in lanthanide systems, in which incoherent MIR radiation directly perturbs the relaxation network governing excited-state populations. In conventional lanthanide photophysics, steady-state population distributions within thermally coupled manifolds follow Boltzmann statistics and are therefore tightly linked to lattice temperature.^{22,31,32} In contrast, our experiments show that MIR irradiation can drive the system into a non-Boltzmann steady state in which dissipative relaxation pathways, rather than thermal equilibrium, govern the population distribution. This photon-driven redistribution relaxes the Boltzmann constraint that typically links emission ratios to temperature, enabling external control of steady-state populations without measurable heating.

The behaviour differs from previously reported MIR-lanthanide interactions, which are predominantly mediated by thermal effect such as ligand-assisted heating or temperature-dependent energy transfer.^{27,28,29} In those cases, MIR absorption modifies lattice temperature and the emission response remains governed by Boltzmann statistics. Here, the response is consistent with a direct modification of multiphonon relaxation processes linking Stark-split sublevels. MIR excitation interacts with the vibrational environment of the host lattice and alters phonon-assisted relaxation rates, leading to strongly state-dependent lifetime renormalization and opposite emission responses within thermally coupled manifolds.³³ Because this process modifies relaxation dynamics rather than excitation pathways, the resulting steady-state population distribution becomes externally controllable while remaining largely decoupled from temperature.

Discussion

In summary, we demonstrate that MIR radiation drives lanthanide nanocrystals into a non-Boltzmann steady state by selectively perturbing phonon-assisted relaxation pathways. This photon-driven rebalancing of relaxation rates alters the population distribution within thermally coupled manifolds and gives rise to opposite emission responses. The resulting population redistribution enables pump-power-independent ratiometric detection of MIR radiation across the 6.8-8.6 μm under microwatt-level near-infrared excitation. Further, the integration with silicon photodetectors allows room-temperature MIR imaging.

The non-Boltzmann response persists at the single-nanocrystal level, indicating that the MIR-induced redistribution originates from intrinsic emitter dynamics rather than ensemble averaging. The sensing modality therefore remains stable over nearly three orders of magnitude of pump power, while maintaining broadband spectral sensitivity and excellent photostability.²⁷ More broadly, the visible upconversion readout provides a direct interface with computational imaging approaches, including structured illumination or single-pixel detection schemes.^{34,35} These findings establish photon-driven control of relaxation dynamics as a route to manipulate steady-state populations beyond thermally governed limits in lanthanide photonics, and suggest opportunities for scalable MIR sensing and imaging.

Online Methods

All the experimental details, including the synthesis of nanocrystals, structural characterization, optical set-up, data acquisition and numerical simulations of the MIR modulation process, are provided in the Supplementary Information.

Data availability

All relevant data that support the findings of this work are available from the corresponding author on reasonable request.

Code availability

All code used in this paper is available from the corresponding authors upon reasonable request.

Acknowledgements

The authors acknowledge financial support from the Australian Research Council (DE250100406, CE200100010, FT220100053) and the Air Force Office of Scientific Research (FA2386-25-1-4044).

Author contributions

C.C. and I.A. designed and conceptualized the research. C.C. and I.A. supervised the work. X.Y. and C.C. built the mid-infrared optical setup. X.Y., C.C., K.Y., M.K. and J.K. performed optical experiments and data analysis. Y.H., G.B. and X.X. synthesized the nanoparticles and performed the electron microscopy imaging. C.W., C.C. and F.W. performed the numerical simulations. L.D., B.L. and O.S. fabricated the nanoscale test chart. X.Y., Y.Y., Y.B., L.F., Y.H. and Q.S. performed the FITR and temperature control measurements. X.Y., C.C. and I.A. wrote the manuscript. All authors discussed the results and revised the manuscript.

Competing interests

The authors declare no competing interests.

Reference

1. Bai, Y., Yin, J. & Cheng, J. Bond-selective imaging by optically sensing the mid-infrared photothermal effect. (2021).
2. Fang, J., Huang, K., Wu, E., Yan, M. & Zeng, H. Mid-infrared single-photon 3D imaging. *Light Sci. Appl.* **12**, 144 (2023).
3. Fang, J. *et al.* Wide-field mid-infrared hyperspectral imaging beyond video rate. *Nat. Commun.* **15**, 1811 (2024).
4. Chikkaraddy, R., Arul, R., Jakob, L. A. & Baumberg, J. J. Single-molecule mid-infrared spectroscopy and detection through vibrationally assisted luminescence. *Nat. Photonics* **17**, 865–871 (2023).
5. Tamamitsu, M. *et al.* Mid-infrared wide-field nanoscopy. *Nat. Photonics* **18**, (2024).
6. Li, Y. *et al.* Mid- - infrared photodetection with 2D metal halide perovskites at ambient temperature. **2778**, 1–11 (2024).

7. Chen, W. *et al.* Enabling highly efficient infrared silicon photodetectors via disordered metasurfaces with upconversion nanoparticles. **7783**, 1–8 (2025).
8. Chen, W. *et al.* Continuous-wave frequency upconversion with a molecular optomechanical nanocavity. *Science*. **374**, 1264–1267 (2021).
9. Xomalis, A. *et al.* Detecting mid-infrared light by molecular frequency upconversion in dual-wavelength nanoantennas. *Scienc*. **374**, 1268–1271 (2021).
10. Zou, F., Du, L., Li, Y. & Dong, H. Amplifying Frequency Up-Converted Infrared Signals with a Molecular Optomechanical Cavity. *Phys. Rev. Lett.* **132**, 153602 (2024).
11. Xie, Z., Oyamada, N., Ciccarello, F., Chen, W. & Galland, C. Continuous-wave, high-resolution, ultra-broadband mid-infrared nonlinear spectroscopy with tunable plasmonic nanocavities. 1–24.
12. Arul, R. *et al.* Giant mid-IR resonant coupling to molecular vibrations in sub-nm gaps of plasmonic multilayer metafilms. *Light Sci. Appl.* **11**, (2022).
13. Chikkaraddy, R., Xomalis, A., Jakob, L. A. & Baumberg, J. J. Mid-infrared-perturbed molecular vibrational signatures in plasmonic nanocavities. *Light Sci. Appl.* **11**, 19 (2022).
14. Jia, D. *et al.* Ultrasensitive infrared spectroscopy via vibrational modulation of plasmonic scattering from a nanocavity. **8255**, 1–10 (2024).
15. Yan, L., Huang, J., An, Z., Zhang, Q. & Zhou, B. Spatiotemporal control of photochromic upconversion through interfacial energy transfer. 1–9 (2024) doi:10.1038/s41467-024-46228-5.
16. Chen, C. *et al.* Heterochromatic Nonlinear Optical Responses in Upconversion Nanoparticles for Super-Resolution Nanoscopy. *Adv. Mater.* **33**, (2021).
17. Ding, L. *et al.* Optical Nonlinearity Enabled Super-Resolved Multiplexing Microscopy. *Adv. Mater.* **36**, 2308844 (2024).
18. Skripka, A. *et al.* Intrinsic optical bistability of photon avalanching nanocrystals. *Nat. Photonics* **19**, (2025).
19. Zhu, S., Pan, T. & Chen, J. Upconversion optical entropy encoding for infrared complex-amplitude imaging. (2026).
20. García-Flores, A. F. *et al.* Crystal-field Stark effect on the upconversion light emission spectrum of α -NaYF₄ nanoparticles doped with Dy³⁺, Er³⁺, or Yb³⁺. *Phys. Rev. B* **106**, (2022).
21. Gruber, J. B. *et al.* Modeling the crystal-field splitting of energy levels of Er³⁺(4f¹¹) in charge-compensated sites of KPb₂Cl₅. *J. Appl. Phys.* **100**, 043108 (2006).
22. Olshin, P. K. *et al.* Boltzmann-Distribution-Driven Cathodoluminescence Thermometry in In Situ Transmission Electron Microscopy. (2024) doi:10.1021/acsnano.4c10126.
23. Pickel, A. D. *et al.* Apparent self-heating of individual upconverting nanoparticle thermometers. *Nat. Commun.* 4907 (2018) doi:10.1038/s41467-018-07361-0.
24. Swieten, T. P. Van *et al.* Extending the dynamic temperature range of Boltzmann thermometers. (2022) doi:10.1038/s41377-022-01028-8.
25. Yu, D., Li, H., Zhang, D. & Suta, M. One ion to catch them all : Targeted high-precision Boltzmann thermometry over a wide temperature range with Gd³⁺. *Light. Appl.* 236 (2021) doi:10.1038/s41377-021-00677-5.
26. Suta, M. What makes β -NaYF₄ Er³⁺, Yb³⁺ such a successful luminescent thermometer. *Nanoscale* 7091–7099 (2025) doi:10.1039/d4nr04392h.
27. Liang, L., Wang, C., Chen, J., Wang, Q. J. & Liu, X. Incoherent broadband mid-infrared detection with lanthanide nanotransducers. doi:10.1038/s41566-022-01042-7.
28. Guan, J. *et al.* Mid- to Long-Wave-Infrared Nanoscopy With Lanthanide Transducers. *Laser Photon. Rev.* 0:e01012 (2025) doi:10.1002/lpor.202501012.
29. Wang, Q. *et al.* Ultrasensitive Mid-Infrared Detection through Ligand-Driven Local Heating in Lanthanide-doped Nanoparticles Ultrasensitive Mid-Infrared Detection through Ligand-Driven Local Heating in Lanthanide-doped Nanoparticles. 0–12 (2025).
30. Zhang, W. *et al.* Multiplexed Single-Particle Imaging Enabled by Modulation of Er³⁺ Energy-Level Populations. **14220**, 1–10 (2025).

31. Kinik, G., Widmann, I., Bendel, B., Huppertz, H. & Meijerink, A. Ratiometric Boltzmann thermometry with Cr³⁺ in strong ligand fields: Efficient nonradiative coupling for record dynamic working ranges. (2025).
32. Pessoa, A. R., Menezes, L. D. S. & Amaral, A. M. Addressing Discrepancies between Theory and Experiments in Boltzmann Luminescence Thermometry with Ln³⁺ Ions. (2025) doi:10.1021/acs.jpcc.5c01864.
33. Skripka, A. Heavy Halide Nanomaterials as Next-Generation Hosts for Lanthanide Upconversion. (2026) doi:10.1021/jacs.5c22136.
34. Edgar, M. P., Gibson, G. M. & Padgett, M. J. Principles and prospects for single-pixel imaging. *Nature Photonics* vol. 13 13–20 at <https://doi.org/10.1038/s41566-018-0300-7> (2019).
35. Wang, Y. *et al.* Mid-infrared single-pixel imaging at the single-photon level. *Nat. Commun.* **14**, 1073 (2023).

Supplementary Information

Harnessing Non-Boltzmann Steady States in Lanthanide Nanocrystals for Mid-Infrared Optoelectronics

Xinyang Yu, Yin Huang, Karin Yamamura, Chengyi Wang, Lei Ding, Mehran Kianinia, Yang Yu, Jiyun Kim, Baolei Liu, Xiaoxue Xu, Otto Cranwell Schaeper, Yue Bian, Lan Fu, Guochen Bao, Qian Peter Su, Fan Wang, Igor Aharonovich*, Chaohao Chen*

Contents

Supplementary Note 1 Experimental setup.....	2
Supplementary Note 2 Nanoparticle synthesis	3
Supplementary Note 3 Numerical simulation.....	5
Supplementary Note 4 Detection performance calculations.....	7
Supplementary Fig. S1.....	8
Supplementary Fig. S2.....	9
Supplementary Fig. S3.....	10
Supplementary Fig. S4.....	11
Supplementary Fig. S5.....	12
Supplementary Fig. S6.....	13
Supplementary Fig. S7.....	14
Supplementary Fig. S8.....	15
Supplementary Fig. S9.....	16
Supplementary Fig. S10.....	17
Supplementary Fig. S11.....	18
Supplementary Fig. S12.....	19
Supplementary Fig. S13.....	20
Supplementary Fig. S14.....	21
Supplementary Fig. S15.....	22
Supplementary Table S1	23

Supplementary Note 1 Experimental setup

All the measurements were performed on a home-built confocal microscope system for mid-infrared co-excitation and upconversion readout. As schematically illustrated in Fig. S1, a single-mode fiber-coupled 980 nm diode laser (BL976- PAG900, controller CLD1015, Thorlabs) was used to excite the UNCPS. After collimation by a lens (L1, F230APC-980, Thorlabs), the excitation beam passed through a half-wave plate (HWP, WPH05M-980, Thorlabs) and a polarized beam splitter (PBS, CCM1-PBS252/M, Thorlabs), which were used to precisely tune the excitation power by electronically rotating the polarization direction of the incident beam. The excitation beam was then reflected by a short-pass dichroic mirror (DM, T875spxrxt-UF1, Chroma) and focused through a high numerical aperture objective (100X OL, MUE13900, Nikon) to the sample slide. The sample was fixed on a XYZ piezo stage (P-6113S NanoCube, PI), enabling precise positioning during both ensemble and single-particle measurements. MIR irradiation was provided by a tunable quantum cascade laser (MIR tunable QCL, MIRcat, Daylight Solutions) operating over the 6.8-8.6 μm wavelength range. The MIR beam was first directed by a gold mirror. It was then modulated by an optical chopper (blade MC1F10HP, controller MC2000B, Thorlabs) at 100HZ and focused onto the sample using a reflective microscope objective with a focal length of 5 mm (LMM40X-P01, Thorlabs). The MIR beam spot was aligned to spatially overlap with the 980 nm excitation spot at the sample plane.

The upconversion fluorescent was collected by the same objective and separated from the excitation beam by the dichroic mirror. The collected emission signals were further passed through a short-pass filter (SPF, FF01-842/SP-25, Semrock) to suppress the residual 980 nm excitation background and then routed by a flip mirror (FM1) into two detection branches. In one branch, the emission was focused by a lens (L2, AC254-200-AB, Thorlabs) and directed by a second flip mirror (FM2) either to a grating spectrometer (QE Pro, Ocean Optics) for spectral acquisition or to a beam splitter (BS, BS016, Thorlabs) for dual-channel photon-counting detection and single-particle scanning imaging. In the latter configuration, the signal was split into two paths and filtered by band-pass filters (BPF1, FF01-525/15-25, Semrock) and (BPF2, FF01-550/32-25, Semrock) to isolate the 525 nm and 545 nm emission bands, which were detected simultaneously by SPAD1 and SPAD2 (SPCM-AQRH-14-FC, Excelitas), respectively. Spectra were typically acquired with an integration time of 10 ms, whereas the pixel dwell time for dual-channel SPAD scanning was set to 40 ms. In the other branch, the luminescence signals were focused by a lens (L3, AC254-200-AB, Thorlabs) onto a variable-gain Si avalanche photodetector (Si APD, APD410A2(/M), Thorlabs) for lock-in-amplified photoresponse measurements. The detector was operated at a gain of 50 dB, corresponding to a responsivity of 12.4×10^6 V/W. The output voltage was first fed into a lock-in amplifier (Signal Recovery, 7270) for demodulation, with the reference provided by the optical chopper and a time constant of 50 ms. The demodulated voltage was then monitored with an oscilloscope (Tektronix, TDS 3014B). The incident MIR power was measured using a thermal power meter (sensor S401C, console PM100D, Thorlabs). Typical excitation powers for the mid-infrared response varied from 10 μW to 500 mW. All powers are measured at the back aperture of the objective lens. This collection architecture enabled flexible switching among spectral measurements, wide-field imaging, lock-in-amplified photoresponse readout, and dual-channel single-particle detection while preserving the same co-excitation geometry.

Supplementary Note 2 Nanoparticle synthesis

1.1 Materials

$\text{ErCl}_3 \cdot 6\text{H}_2\text{O}$ (99.9%), $\text{YCl}_3 \cdot 6\text{H}_2\text{O}$ (99.9%), $\text{YbCl}_3 \cdot 6\text{H}_2\text{O}$ (99.9%), oleic acid (OA, 90%), and 1-octadecene (ODE, 90%) were purchased from Sigma-Aldrich. NH_4F (96.0%), NaOH (98.0%) and cyclohexane (99.9%) were purchased from ChemSupply. Absolute ethanol (100%) and methanol (100%) were purchased from Point of Care Diagnostics. All chemicals, reagents, and solvents were purchased commercially and used as received without any further treatment.

1.2 Synthesis of $\text{NaYF}_4: 20\% \text{Yb}^{3+}, 2\% \text{Er}^{3+}$ nanoparticles

The $\text{NaYF}_4: 20\% \text{Yb}^{3+}, 2\% \text{Er}^{3+}$ nanoparticles were synthesized using a co-precipitation method.¹ In a typical procedure, a methanol solution containing 1 mmol of $\text{YCl}_3 \cdot 6\text{H}_2\text{O}$, $\text{YbCl}_3 \cdot 6\text{H}_2\text{O}$, and $\text{ErCl}_3 \cdot 6\text{H}_2\text{O}$ together with 6 mL of OA and 15 mL of ODE were added to a 50 mL three-neck round-bottom flask under vigorous stirring. The resulting mixture was heated to 150 °C for 30 min to form lanthanide oleate complexes. The solution was cooled down to room temperature. Subsequently, a methanol solution containing 2.5 mmol of NaOH and 4 mmol of NH_4F was added and stirred at room temperature for 30 min, and then the mixture was slowly heated to 90 °C and kept for 30 min under argon flow to remove methanol and residual water. Next, the solution was quickly heated to 300 °C under argon flow for 90 min before cooling down to room temperature. The resulting core nanoparticles were precipitated by the addition of ethanol and collected by centrifugation at 9000 rpm for 10 min. After being washed several times with cyclohexane and ethanol, the final $\text{NaYF}_4: 20\% \text{Yb}^{3+}, 2\% \text{Er}^{3+}$ nanocrystals were dispersed in cyclohexane.

Using the same method, we also synthesized several other core nanoparticles with different Er^{3+} doping concentrations (0.5%-8%), including $\text{NaYF}_4: 20\% \text{Yb}^{3+}, 0.5\% \text{Er}^{3+}$, $\text{NaYF}_4: 20\% \text{Yb}^{3+}, 4\% \text{Er}^{3+}$, and $\text{NaYF}_4: 20\% \text{Yb}^{3+}, 8\% \text{Er}^{3+}$.

1.3 Synthesis of $\text{NaYF}_4: 20\% \text{Yb}^{3+}, 2\% \text{Er}^{3+} @ \text{NaYF}_4$ nanoparticles

$\text{NaYF}_4: 20\% \text{Yb}^{3+}, 2\% \text{Er}^{3+} @ \text{NaYF}_4$ nanoparticles were synthesized by growth of a shell precursor on core nanoparticles via a hot-injection method.² The first step involved the preparation of the shell precursor. 1 mmol of $\text{YCl}_3 \cdot 6\text{H}_2\text{O}$ was added to a 50 mL flask containing 6 mL of OA and 15 mL of ODE. The mixture was heated to 160 °C under argon for 30 min to obtain a transparent solution and then cooled down to room temperature, followed by the addition of 10 mL methanol solution containing NaOH (2.5 mmol) and NH_4F (4 mmol). After that, the solution was heated to 90 °C under an argon atmosphere for 30 min to remove methanol, and then the temperature was raised to 160 °C for 30 min to form a clear solution. Finally, the solution was cooled down to room temperature and designated as shell precursors.

In the second step, 0.2 mmol of $\text{NaYF}_4: 20\% \text{Yb}^{3+}, 2\% \text{Er}^{3+}$ nanoparticles, 6 mL of OA, and 6 mL of ODE were added to a 50 mL three-neck round-bottom flask. The mixture was heated to 300 °C under argon flow. Then, 3 mL of the NaYF_4 shell precursor was injected into the reaction mixture. After the reaction, the mixture was cooled to room temperature and purified several times by centrifugation, dispersing it in cyclohexane for further use.

1.4 Preparation of Ligand-Free Nanoparticles

After washing with ethanol and cyclohexane, the $\text{NaYF}_4: 20\% \text{Yb}^{3+}, 2\% \text{Er}^{3+}$ nanoparticles were dispersed in cyclohexane at a concentration of 6 mg mL⁻¹. The OA ligands on the nanoparticle surface were removed according to a modified literature procedure.³ A 0.75 mL aliquot of the nanoparticle dispersion was mixed with 0.75 mL of ethanol, ultrasonicated for 5 min, and then centrifuged at 10,000 rpm for 15 min. The resulting precipitate was redispersed in a mixture of 0.75 mL of HCl (2M) and 0.75 mL of ethanol, followed by centrifugation at 10,000 rpm for 30 min. Stepwise solvent exchange was then carried out using ethanol/water mixtures of 0.75/0.75 mL and 0.25/1.25 mL, respectively, with centrifugation at 10,000 rpm for 30 min after

each step. Finally, the nanoparticles were redispersed in 1.5 mL of water.

1.5 Characterization techniques

The morphology of the as-synthesized nanoparticles was characterized using Transmission Electron Microscopy (TEM, JEOL F200) operated at an accelerating voltage of 200 kV. The samples were prepared by drop-casting a dilute nanocrystal suspension onto copper grids. High resolution TEM (HRTEM) images were taken at high magnification using JEOL F200 at 200 kV to examine the crystallinity of the synthesized nanoparticles. Crystal phase analysis of the nanoparticles was applied using a Bruker D8 Discover A25 X-ray diffractometer (XRD) with Cu K α radiation (40 kV, 40 mA, $\lambda = 0.15406$ nm). The XRD spectra were compared to the standard file of NaYF₄ (PDF 00-048-185) to identify the crystal phase and structure.

Supplementary Note 3 Numerical simulation

3.1 Reduced kinetic model for MIR-driven population redistribution

Under 980 nm excitation, visible upconversion emission in $\text{Yb}^{3+}/\text{Er}^{3+}$ nanocrystals arises from three emitting manifolds: $^2\text{H}_{11/2}$ (525 nm), $^4\text{S}_{3/2}$ (545 nm), and $^4\text{F}_{9/2}$ (660 nm). The populations of these manifolds are denoted as N_7 , N_6 , and N_5 , respectively.

Rather than reconstructing the full microscopic $\text{Yb}^{3+}/\text{Er}^{3+}$ excitation ladder, we adopt a coarse-grained kinetic description that focuses only on the population dynamics of these experimentally observed emitting levels. Higher-lying manifolds and intermediate excitation pathways are incorporated into effective injection terms G_i , representing the net population flow into each emitting state under continuous 980 nm pumping.

Within this framework, MIR illumination is introduced as a perturbation of the dissipative relaxation network rather than as an additional optical excitation channel. Specifically, MIR radiation modifies the effective decay rates of the emitting manifolds and introduces a redistribution pathway between the thermally coupled green states.

The population dynamics are described by

$$\begin{aligned}\frac{dN_6}{dt} &= G_6 - [\Gamma_{6,off} + \Delta K_6(P) + W_{MIR}(P)]N_6 \\ \frac{dN_7}{dt} &= G_7 - [\Gamma_{7,off} + \Delta K_7(P)]N_7 + W_{MIR}(P)N_6 \\ \frac{dN_5}{dt} &= G_5(P) - [\Gamma_{5,off} + \Delta K_5(P)]N_5\end{aligned}$$

where $\Gamma_{i,off}$: intrinsic decay rate; $\Delta K_i(P)$: MIR-induced decay-rate modification; $W_{MIR}(P)$: MIR-driven redistribution rate between the green manifolds.

This reduced kinetic model directly describes the dynamics of the experimentally observed emission channels while avoiding the parameter non-uniqueness associated with full multilevel upconversion models.

3.2 Extraction of MIR-induced decay-rate renormalization

The MIR-induced modification of the relaxation network is quantified through lifetime measurements performed with and without MIR illumination.

For each emitting manifold, the effective decay rate is

$$\Gamma_i = 1/\tau_i$$

The MIR-induced change in the decay rate is

$$\Delta K_i(P) = \frac{1}{\tau_{i,on}} - \frac{1}{\tau_{i,off}}$$

These measurements reveal strongly state-dependent rate renormalization under MIR illumination. In particular, the $^4\text{F}_{9/2}$ manifold exhibits the largest lifetime reduction, indicating that MIR irradiation selectively perturbs specific nonradiative relaxation pathways.

In the low-power regime, the MIR-induced rate modification can be approximated as

$$\Delta K_i(P) \approx \alpha_i(P)$$

where α_i is obtained from the experimentally measured slope of ΔK_i versus MIR power.

3.3 MIR-induced redistribution within the thermally coupled green manifolds

The experimentally observed opposite responses of the 525 nm and 545 nm emission bands indicate population redistribution within the thermally coupled green manifolds.

To capture this behavior, we introduce a MIR-dependent redistribution channel

$$N_6 W_{MIR}(P) \rightarrow N_7$$

with rate $W_{MIR}(P)$.

In the low-power regime this rate is modeled as

$$W_{MIR}(P) = \beta P$$

More generally, a weakly saturating form may also be used

$$W_{MIR}(P) = \frac{\beta P}{1 + P/P_{sat}}$$

This term phenomenologically represents MIR-induced modification of phonon-assisted relaxation pathways linking the two green manifolds.

3.4 Steady-state solutions and ratiometric response

At steady state

$$\frac{dN_i}{dt} = 0$$

the populations become

$$N_6(P) = \frac{G_6}{\Gamma_{6,off} + \Delta K_6(P) + W_{MIR}(P)}$$

$$N_7(P) = \frac{G_7 + W_{MIR}(P)N_6(P)}{\Gamma_{7,off} + \Delta K_7(P)}$$

$$N_5(P) = \frac{G_5(P)}{\Gamma_{5,off} + \Delta K_5(P)}$$

The experimentally measured ratiometric signal is therefore

$$R(P) = \frac{I_{525}(P)}{I_{545}(P)} = \frac{N_7(P)}{N_6(P)}$$

This expression describes how MIR-induced rate renormalization and redistribution jointly determine the observed ratiometric response.

3.5 Effective violation of local detailed balance

In the absence of MIR illumination, the thermally coupled green manifolds satisfy detailed balance through phonon-assisted relaxation processes.

Denoting the thermal forward and backward rates as

$$\frac{k_{6 \rightarrow 7}^{th}}{k_{7 \rightarrow 6}^{th}} = e^{-\Delta E/k_B T}$$

Under MIR illumination, the effective forward redistribution rate becomes

$$k_{6 \rightarrow 7}^{eff} = k_{6 \rightarrow 7}^{th} + W_{MIR}(P)$$

while

$$k_{7 \rightarrow 6}^{eff} \approx k_{7 \rightarrow 6}^{th}$$

Therefore

$$\frac{k_{6 \rightarrow 7}^{th}}{k_{7 \rightarrow 6}^{th}} \neq e^{-\Delta E/k_B T}$$

This indicates that local detailed balance within the thermally coupled green manifold is effectively violated. Although the system still reaches a steady state, the population distribution is no longer governed by Boltzmann statistics.

Instead, a persistent redistribution flux

$$J_{6 \rightarrow 7} = W_{MIR}(P)N_6$$

is maintained by the MIR field, leading to a driven nonequilibrium steady state.

Supplementary Note 4 Detection performance calculations

4.1 Excitation power density

For ease of sample access and alignment during the ensemble measurements, the reflective objective used in the confocal configuration was replaced by a ZnSe plano-convex lens with a focal length of 60 mm for MIR focusing. Under this geometry, the MIR beam was focused onto the sample using the ZnSe lens, and the corresponding MIR power density at the sample plane was estimated from the measured MIR power and the calculated focal spot area.

The MIR beam was approximated as a Gaussian beam with a wavelength of $\lambda = 8.0 \mu\text{m}$ and an incident beam diameter of $D = 5 \text{ mm}$. Under the Gaussian-beam approximation, the beam waist at focus is given by

$$\omega = \frac{2\lambda f}{\pi D}$$

where ω is the beam waist radius, f is the focal length of the ZnSe lens and D is the incident beam diameter. Substituting the corresponding values gives

$$\omega = \frac{2 \times 8.0 \times 60000}{\pi \times 5000} \approx 61.1 \mu\text{m}$$

Accordingly, the effective focal area was estimated as

$$A = \pi \times (61.1)^2 \approx 1.17 \times 10^4 \mu\text{m}^2$$

4.2 Limit of detection

The mid-infrared detection limit was evaluated from the power-dependent response of the 525/545 nm intensity ratio. Here, the limit of detection (LOD) was defined as the minimum detectable signal corresponding to a signal-to-noise ratio of 1, and was calculated using

$$LOD = \frac{\sigma}{k}$$

where σ represents the standard deviation of the baseline signal measured in the absence of MIR irradiation, and k is the slope extracted from the linear fit of the infrared response as a function of incident MIR power density. Here, the standard deviation of the MIR-off baseline was taken to be

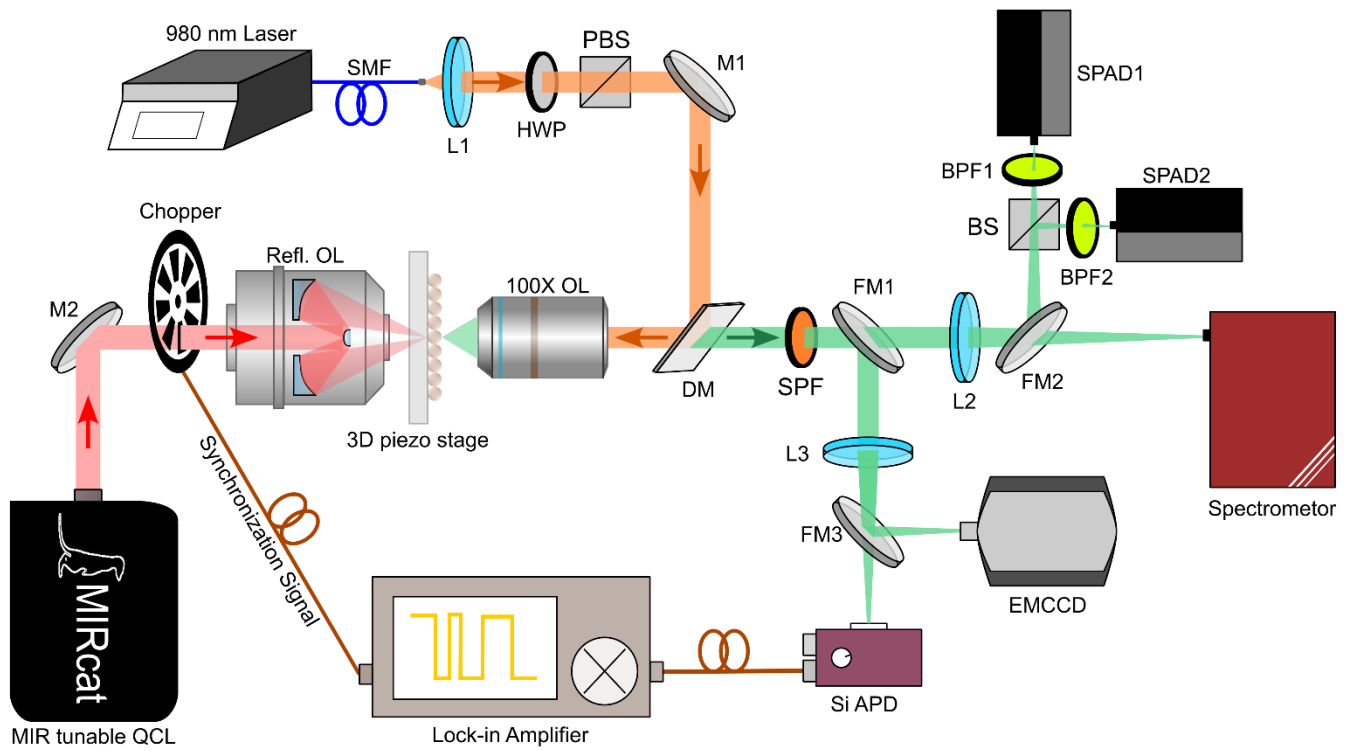
$$\sigma = 0.00105$$

and the slope determined from the linear fit of the full power-dependent dataset was

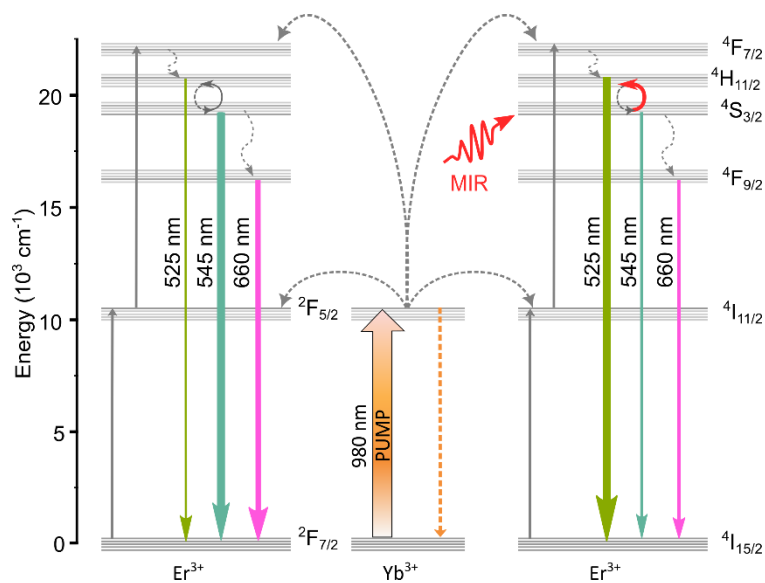
$$k = 0.0212 \text{ mW}^{-1}$$

Using the focal area estimated above, the corresponding power-density detection limit is

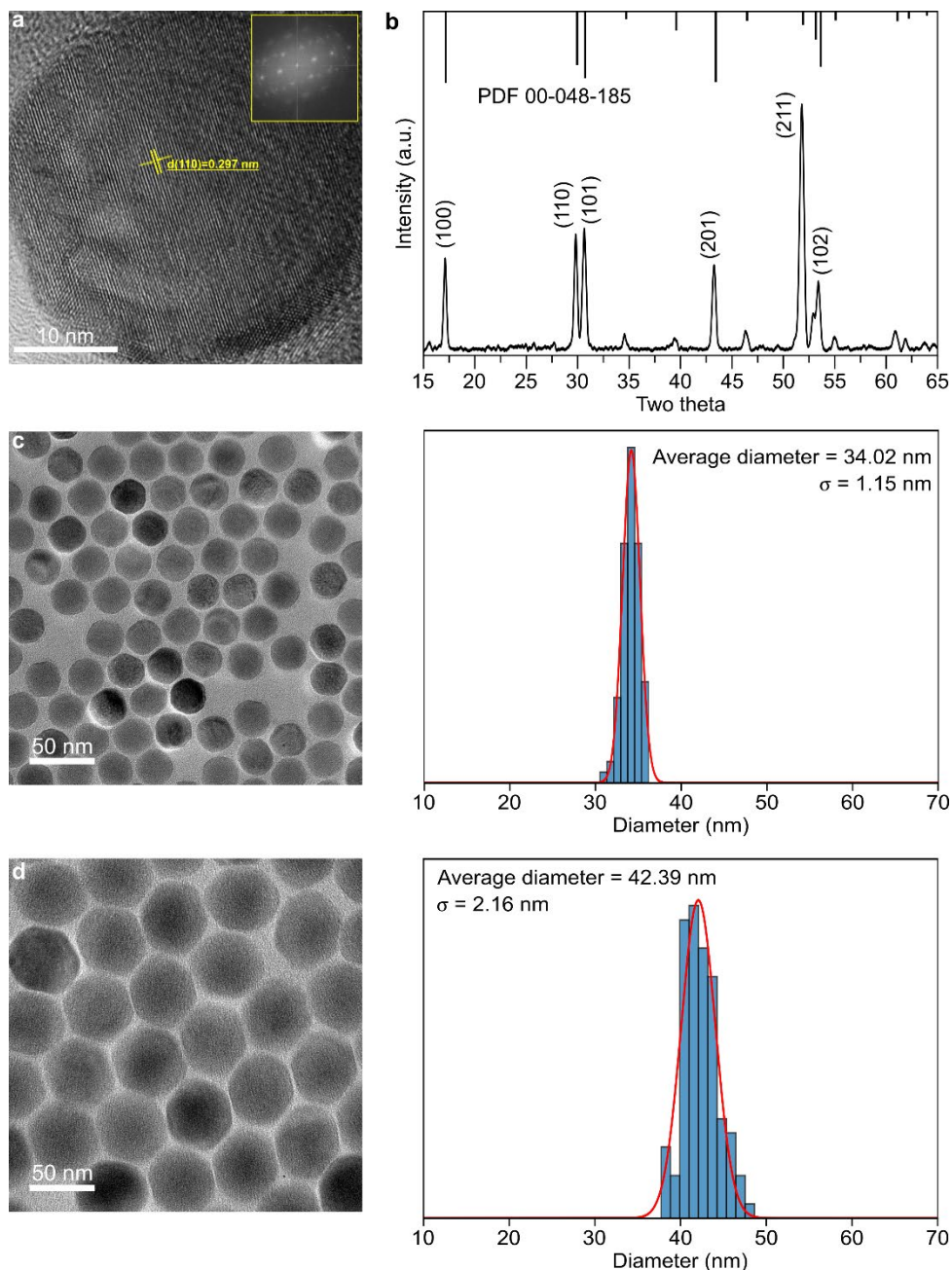
$$LoD \approx 4.0 \text{ nW} / \mu\text{m}^2$$



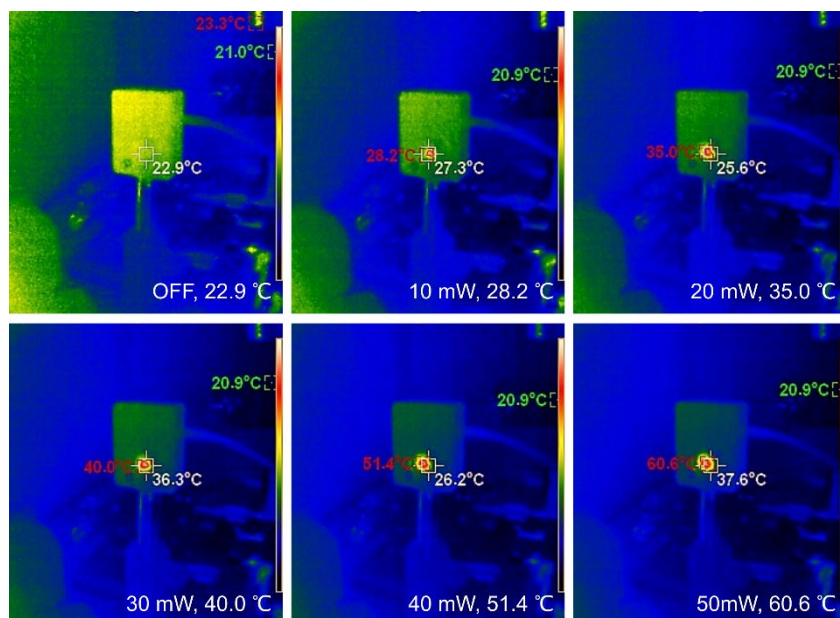
Supplementary Fig. S1 | Schematic of the experimental setup used for MIR-modulated upconversion measurements. SMF, single-mode fiber; L1, collimation lens; HWP, half-wave plate; PBS, polarized beam splitter; M, mirror; DM, dichroic mirror; 100X OL, 100X objective lens; Refl. OL, reflective objective lens; SPF, short-pass filter; L2 and L3, collection lens; FM, flexible mirror; BS, beam splitter; BPF1 and BPF2, band-pass filter; SPAD1 and SPAD2, single-photon avalanche diode; EMCCD, electron-multiplying charge-coupled device; Si APD, Si avalanche photodetector; MIR tunable QCL, mid-infrared tunable quantum cascade laser.



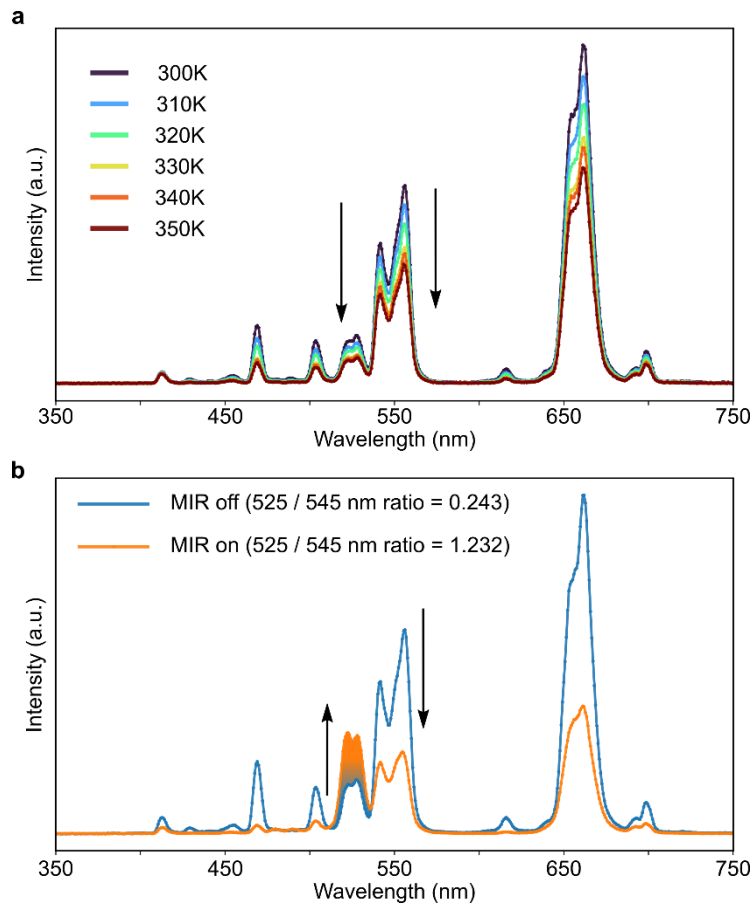
Supplementary Fig. S2 | Schematic energy-level diagram of NaYF₄: Yb³⁺/Er³⁺. Under 980 nm excitation, energy is transferred from Yb³⁺ to Er³⁺, populating the excited states that give rise to the 525 nm, 545 nm, and 660 nm emissions. MIR irradiation perturbs the relaxation pathways among the excited states, leading to a redistribution of populations and a change in the emission ratio.



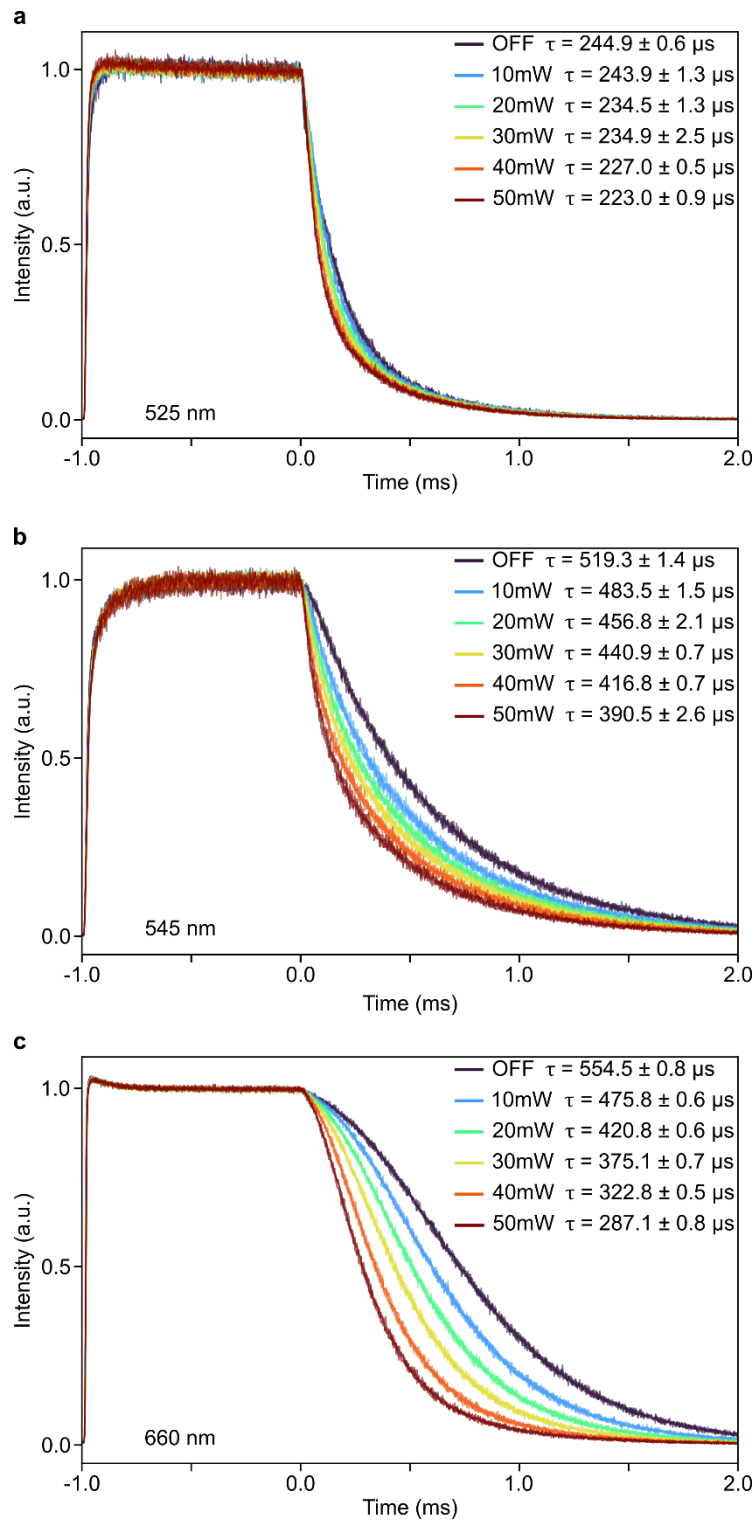
Supplementary Fig. S3 | Structural characterization of the nanocrystals. (a) High-resolution TEM (HRTEM) image displaying clear lattice fringes with an interplanar spacing of 0.297 nm, corresponding to the (110) plane. The inset shows the corresponding fast Fourier transform (FFT) pattern. (b) X-ray diffraction (XRD) pattern confirming the crystalline phase of the nanoparticles, with diffraction peaks indexed to hexagonal β -NaYF₄. (c) TEM images and size distribution of NaYF₄: 20%Yb³⁺/2%Er³⁺. (d) TEM images and size distribution of NaYF₄: 20%Yb³⁺/2%Er³⁺@NaYF₄.



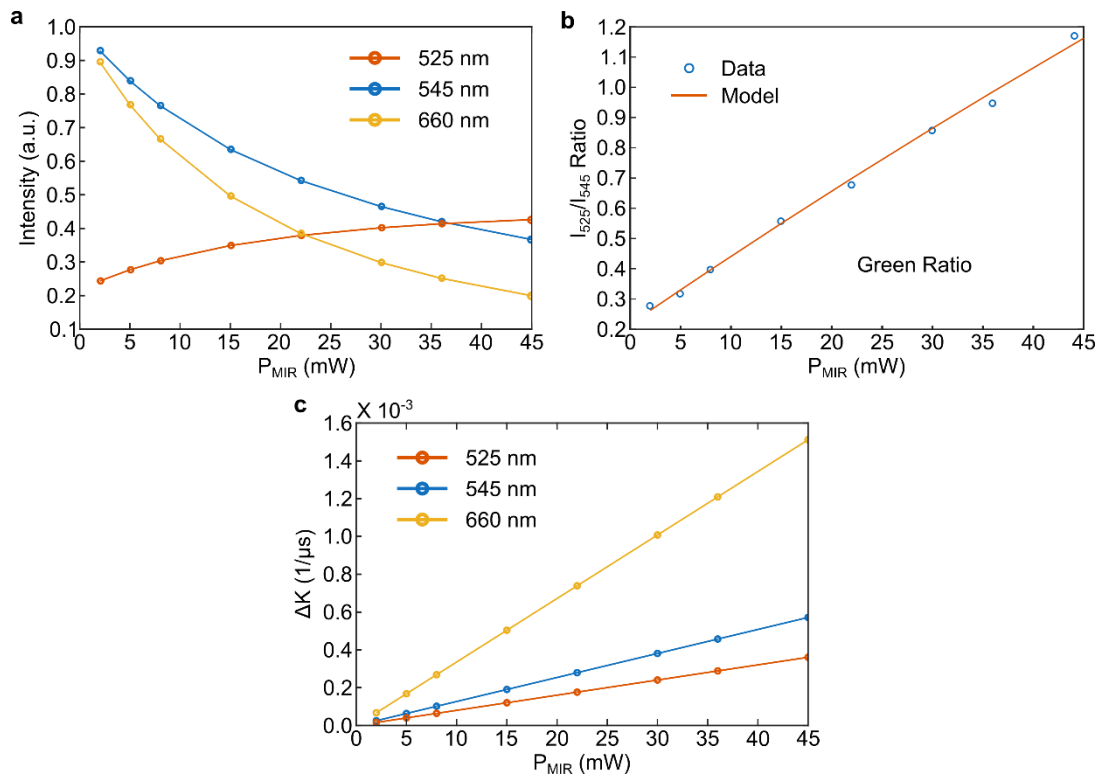
Supplementary Fig. S4 | Thermal images recorded for lanthanide nanocrystal film under different MIR power radiation from 0 mW to 50 mW.



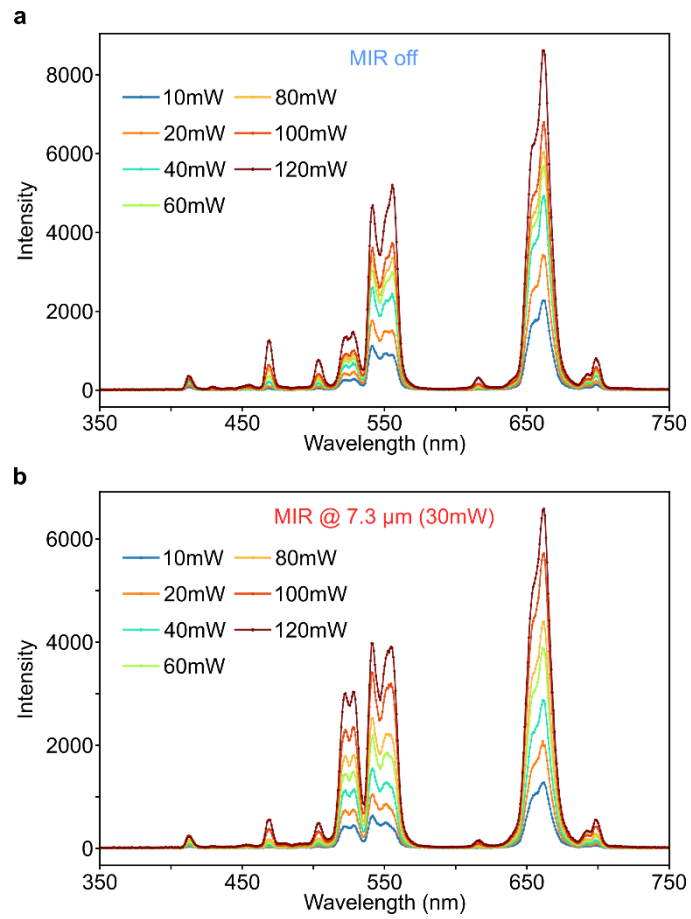
Supplementary Fig. S5 | Temperature-dependent and MIR-induced upconversion spectra of $\text{NaYF}_4:20\%\text{Yb}^{3+}/2\%\text{Er}^{3+}$. (a) Temperature-dependent emission spectra of Er^{3+} from 300 to 350 K. Arrows indicate the same intensity variation of the two green emission bands. (b) Upconversion spectra measured with and without MIR irradiation. The MIR field modifies the relative intensities of the two green emission bands, resulting in a change in the I_{525}/I_{545} ratio.



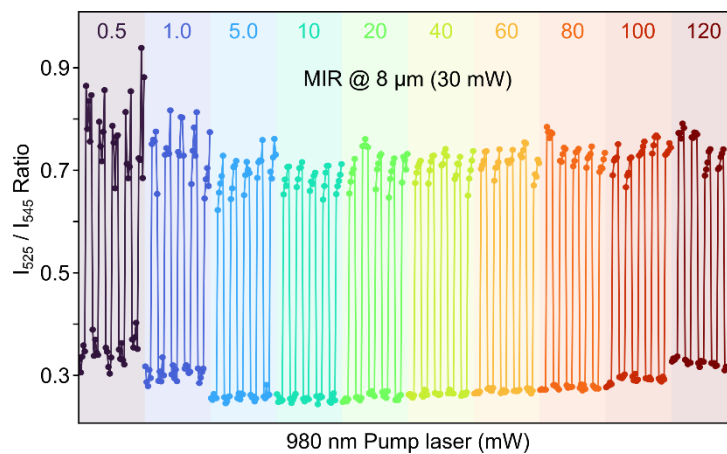
Supplementary Fig. S6 | MIR-induced lifetime modulation of different emission bands. (a)-(c) Time-resolved emission decays of the 525 nm, 545 nm, and 660 nm bands measured under different MIR powers, respectively. The lifetimes show different sensitivities to MIR irradiation, indicating state-selective modulation of excited-state dynamics.



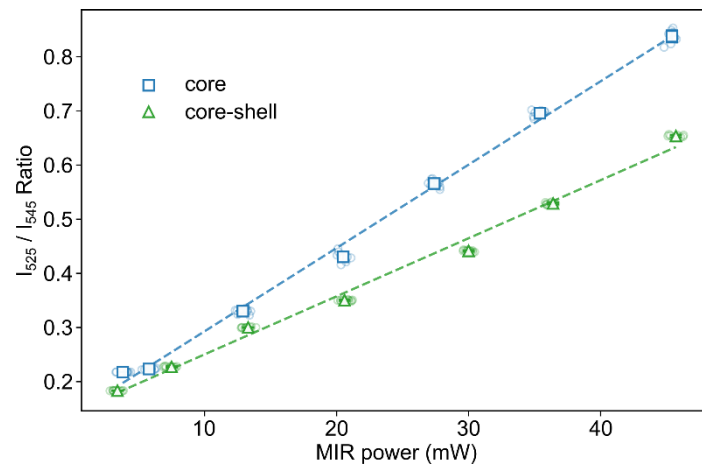
Supplementary Fig. S7 | Rate-equation modelling of the MIR-driven non-Boltzmann steady state. (a) Simulated emission intensities of the 525 nm, 545 nm, and 660 nm bands as a function of MIR power, showing opposite responses within the thermally coupled green manifold. (b) Simulated ratiometric response (I_{525}/I_{545}) exhibiting a linear dependence on MIR power, consistent with experiment. (c) MIR-induced change in inverse lifetime (ΔK) for different emitting levels, revealing a hierarchy of rate enhancement across energy levels.



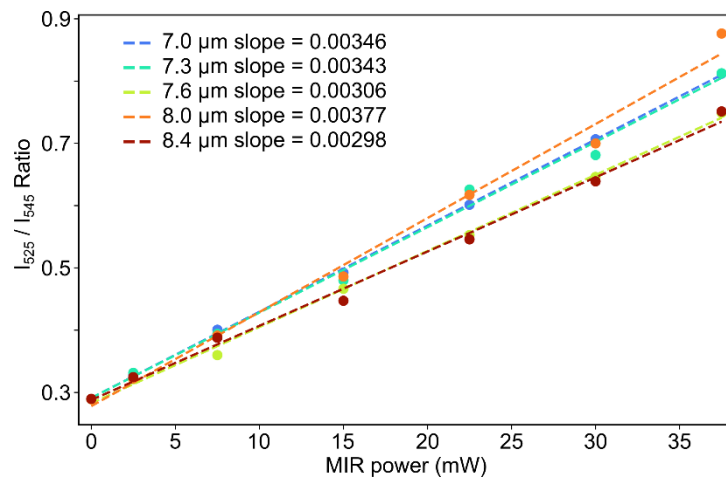
Supplementary Fig. S8 | Pump-power-dependent upconversion spectra with and without MIR irradiation. (a) Upconversion emission spectra under 980 nm excitation with pump powers from 10 to 120 mW without MIR irradiation. (b) Corresponding spectra under MIR irradiation at 7.3 μm (30 mW).



Supplementary Fig. S9 | Reproducibility of the ratiometric response under MIR irradiation. The emission intensity ratio I_{525}/I_{545} measured as a function of 980 nm pump power (0.5-120 mW) under MIR excitation at 8 μm (30 mW). Repeated measurements demonstrate the stability and reproducibility of the ratiometric signal.

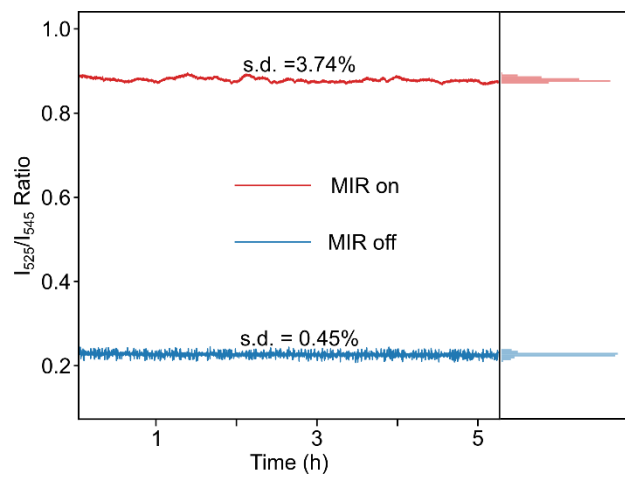


Supplementary Fig. S10 | MIR-induced ratiometric response of core and core-shell nanocrystals. Emission ratio I_{525}/I_{545} as a function of MIR power under identical 980 nm excitation. Both samples show a linear response, while the core-shell nanocrystals exhibit a reduced modulation amplitude.

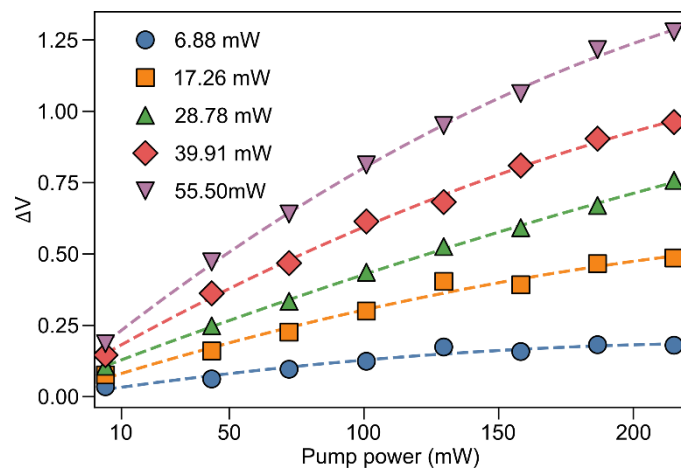


Supplementary Fig. S11 | MIR power-dependent ratiometric response at different MIR wavelengths.

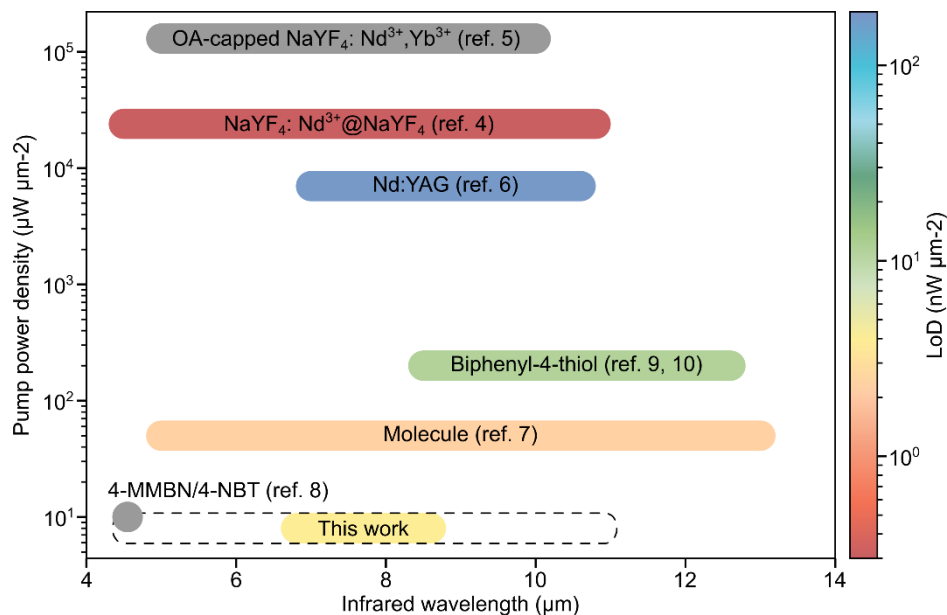
The emission intensity ratio I_{525}/I_{545} plotted as a function of MIR power for wavelengths between 7.0 and 8.4 μm . The ratio increases linearly with MIR power at all wavelengths. Dashed lines show linear fits to the experimental data.



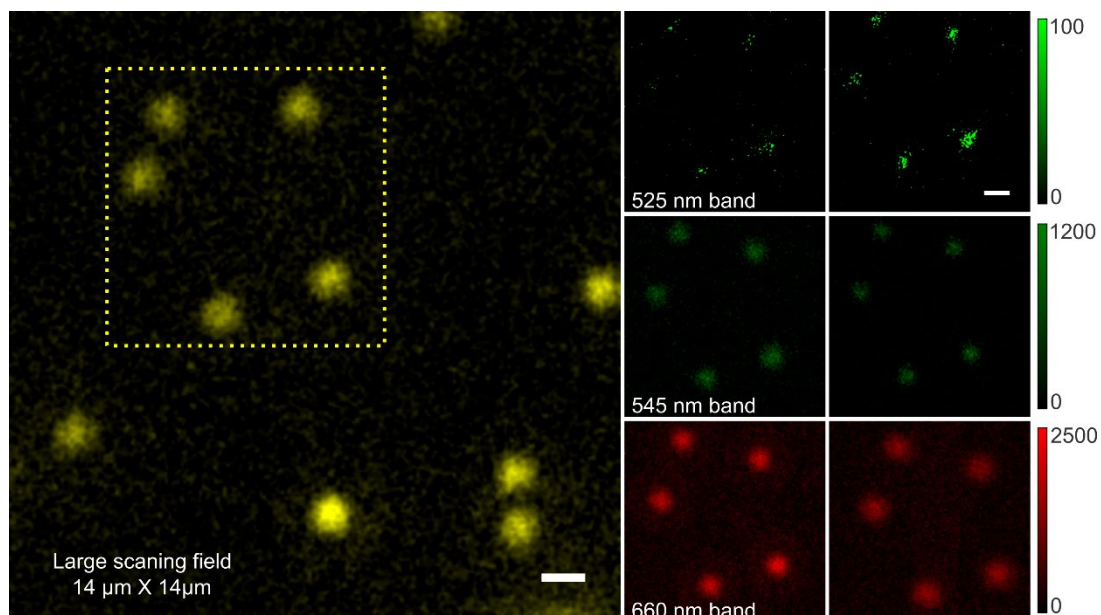
Supplementary Fig. S12 | Long-term stability of the ratiometric signal under continuous operation. Under continuous 980 nm excitation with MIR co-irradiation, the emission ratio from a fixed spot remains stable for over 5 hours with a standard deviation of 3.74% (MIR on) and 0.45% (MIR off), respectively.



Supplementary Fig. S13 | Pump-power-dependent voltage response under different MIR powers. The voltage change (ΔV) as a function of 980 nm pump power measured under different MIR powers. The response increases with pump power and gradually approaches saturation.



Supplementary Fig. S14 | Performance comparison of MIR detection platforms. Comparison of pump power density and working wavelength for different MIR detection approaches. The color scale represents the limit of detection (LoD). The present work operates at significantly lower pump power density while maintaining competitive performance.



Supplementary Fig. S15 | Single-particle emission response under MIR irradiation. Wide-field image of individual nanoparticles and emission maps for the 525 nm, 545 nm, and 660 nm bands. Upon MIR irradiation, the 525 nm emission increases whereas the 545 nm and 660 nm emissions decrease, confirming that the mechanism persists at the single-particle level.

Supplementary Table S1 | Performance comparison among room temperature MIR upconversion materials systems.

materials	Working wavelength (μm)	LoD	Converted wavelength (nm)	Pump density	Imaging	Ref.
NaYF ₄ :Yb ³⁺ , Er ³⁺	6.8-8.6	4 nW/ μm^2	525/545	7 $\mu\text{W}/\mu\text{m}^2$	sub- μm	This work
NaYF ₄ :Nd ³⁺ @NaYF ₄	4.5-10.8	0.3 nW/ μm^2	806/866	24 mW/ μm^2	1 mm	4
OA-capped NaYF ₄ :Nd ³⁺ , Yb ³⁺	5-10	NA	806/980	130 mW/ μm^2	NA	5
Nd:YAG	7-10.6	188 nW/ μm^2	810/890	7 mW/ μm^2	sub- μm	6
Molecule	5-13	2.5 nW/ μm^2	680	50 $\mu\text{W}/\mu\text{m}^2$	NA	7
4-MMBN / 4-NBT	4.55/7.52	NA	638	10 $\mu\text{W}/\mu\text{m}^2$	NA	8
Biphenyl-4-thiol	8.5-12.6	12 nW/ μm^2	785	200 $\mu\text{W}/\mu\text{m}^2$	NA	9,10
LiNbO ₃	3.015-3.17	NA	~771	NA	125 μm	11
2D-MHPs	2-4.5/10.6	10 pW/ μm^2	500	NA	NA	12
CdSe/CdS/ZnS quantum dots	0.2-3	NA	605	NA	~220 μm	13

Reference

- 1 Liu, Y. *et al.* Stabilizing Dye-Sensitized Upconversion Hybrids by Cyclooctatetraene. *Nano Letters* **24**, 12486-12492 (2024).
- 2 Huang, D., Li, F., Ågren, H. & Chen, G. Inhibiting concentration quenching in Yb³⁺-Tm³⁺ upconversion nanoparticles by suppressing back energy transfer. *Nature Communications* **16**, 4218 (2025).
- 3 Tian, J. *et al.* Intracellular adenosine triphosphate deprivation through lanthanide-doped nanoparticles. *Journal of the American Chemical Society* **137**, 6550-6558 (2015).
- 4 Liang, L., Wang, C., Chen, J., Wang, Q. J. & Liu, X. Incoherent broadband mid-infrared detection with lanthanide nanotransducers. *Nature Photonics* **16**, 712-717 (2022).
- 5 jie Wang, Q. *et al.* Ultrasensitive Mid-Infrared Detection through Ligand-Driven Local Heating in Lanthanide-doped Nanoparticles. (2025). <https://doi.org/10.21203/rs.3.rs-6703068/v1>
- 6 Guan, J. *et al.* Mid-to Long-Wave-Infrared Nanoscopy With Lanthanide Transducers. *Laser & Photonics Reviews*, e01012 (2025).
- 7 Chikkaraddy, R., Arul, R., Jakob, L. A. & Baumberg, J. J. Single-molecule mid-infrared spectroscopy and detection through vibrationally assisted luminescence. *Nature Photonics* **17**, 865-871 (2023).
- 8 Jia, D. *et al.* Ultrasensitive infrared spectroscopy via vibrational modulation of plasmonic scattering from a nanocavity. *Science Advances* **10**, eadn8255 (2024).
- 9 Chen, W. *et al.* Continuous-wave frequency upconversion with a molecular optomechanical nanocavity. *Science* **374**, 1264-1267 (2021).
- 10 Xomalis, A. *et al.* Detecting mid-infrared light by molecular frequency upconversion in dual-wavelength nanoantennas. *Science* **374**, 1268-1271 (2021).
- 11 Huang, K., Fang, J., Yan, M., Wu, E. & Zeng, H. Wide-field mid-infrared single-photon upconversion imaging. *Nature communications* **13**, 1077 (2022).
- 12 Li, Y. *et al.* Mid-infrared photodetection with 2D metal halide perovskites at ambient temperature. *Science Advances* **10**, eadk2778 (2024).
- 13 Shi, J. *et al.* A room-temperature polarization-sensitive CMOS terahertz camera based on quantum-dot-enhanced terahertz-to-visible photon upconversion. *Nature nanotechnology* **17**, 1288-1293 (2022).